UC San Diego

UC San Diego Electronic Theses and Dissertations

Title

X-ray and Neutron Scattering Studies of Magnetic Domain Dynamics and Spin Structures

Permalink

https://escholarship.org/uc/item/1nh0h6z1

Author

Chen, San-Wen

Publication Date

2014

Peer reviewed|Thesis/dissertation

eScholarship.org Powered by the California Digital Library
University of California

UNIVERSITY OF CALIFORNIA, SAN DIEGO

X-ray and Neutron Scattering Studies of Magnetic Domain Dynamics and Spin Structures

A dissertation submitted in partial satisfaction of the
requirements for the degree
Doctor of Philosophy

in

Physics

by

San-Wen Chen

Committee in charge:

Professor Sunil Sinha, Chair
Professor Eric Fullerton
Professor Brian Maple
Professor Shirley Meng
Professor Oleg Shpyrko

2014

Copyright
San-Wen Chen, 2014
All rights reserved.

The dissertation of San-Wen Chen is approved, and it is acceptable in quality and form for publication on microfilm and electronically:

_____

_____

_____

_____

_____

Chair

University of California, San Diego

2014

TABLE OF CONTENTS

LIST OF FIGURES

LIST OF TABLES

ACKNOWLEDGEMENTS

First of all, I would like to thank my thesis advisor, Professor Sunil Sinha, for his constant support and useful guidance throughout my graduate study. He is always patient and encouraging when delivering his knowledge through discussions. He is not only a mentor but also like father to me. His serious attitude toward science and his wisdom toward life will always benefit me in the future.

This thesis work has been done with many collaborators and I owe them all a big thank you. I would like to thank Dr. Sujoy Roy, Prof. Karine Dumesnil and Prof. Ami Berkowitz who provide their enormous amount of time and knowledge to my research projects. I would also like to thank my collaborators Dr. Hongyu Guo, Dr. Xiangshun Lu, Dr. Elizabeth Blackburn and Dr. Edwin Fohtung who provide very useful discussions and teach me how to use various experimental tools. My collaborators, Jimmy Kan, Nasim Eibagi, Sergio Montana, Jonathan Sapan, Keith Chan, Sebastian Dietze and Jongwoo Kim, they all contribute to the research works and being good friends. I would also like to thank Prof. Brian Maple, Prof. Eric Fullerton, Prof. Oleg Shpyrko and Prof. Shirley Meng for their interest to serve as my thesis committee members.

The experiments were carried out at many synchrotron sources and neutron sources in various national laboratories. I would like to thank all the scientists in the laboratories, Keoki Seu, Valeria Lauter, Haile Ambaye, Jarek Majewski, Michael Jablin, Michael Sprung and Cecilia Sanchez Hanke, who provided support and made the experiments possible. The research works at UCSD were supported by Basic Energy Sciences, U.S. Dept. of Energy under Grant Number: DE-SC0003678.

I am also grateful to my lab mates, Yicong Ma, Sajal Ghosh, Michael Ip, Ben Holladay, Yi Yang and Jing-Jin Song, who together make a great team and create a happy working environment.

Finally, I would like to thank my beloved family. My parents always provide me with support and encouragement. My wife, Yeling Dai, went through everything with me in the past few years and also provide help in my graduate study.

The text in Chapter 3 is based on the material published in

S. -W. Chen, H. Huo, K. A. Seu, K. Dumesnil, S. Roy and S. K. Sinha. Jamming behavior of domains in a spiral antiferromagnetic system. *Phys. Rev. Lett.*, 110, 217201 (2013).

The text in Chapter 4 is a reprint of the material in

S. -W. Chen, X. Lu, E. Blackburn, V. Lauter, H. Ambaye, K. T. Chan, E. E. Fullerton, A. E. Berkowitz and S. K. Sinha. Non-switchable Magnetic Moments in Polycrystalline and (111)-epitaxial Permalloy/CoO Exchange-biased Bilayers, in preparation (2013).

The content of Chapter 5 is an ongoing project with great help from Jarek Majewski and Michael Jablin in Los Alamos National Laboratory. The extension of the work is in collaboration with Prof. Ivan Schuller, Carlos Monton, Juan Pereiro Viterbo and Ilya Valmianski.

VITA

2002	B. S. in Physics, National Tsing-Hua University, Hsinchu, Taiwan
2004	M. S. in Physics, National Tsing-Hua University, Hsinchu, Taiwan
2008	National School on Neutron and X-ray Scattering, Argonne National Laboratory, Chicago, Illinois
2014	Ph. D. in Physics, University of California, San Diego

PUBLICATIONS

Y. Kuang, S. -W. Chen, H. Li, S. K. Sinha and C. W. Tu, "Growth of $GaN_xAs_yP_{1-x-y}$ Alloys on GaP(100) by Gas-source Molecular Beam Epitaxy", *J. Vac. Sci. Technol., B.*, 30, 02B121, 2011.

S. -W. Chen, H. Guo, K. A, Seu, K. Dumesnil, S. Roy and S. K. Sinha, "Jamming Behavior of Domains in a Spiral Antiferromagnetic System", *Phys. Rev. Lett.*, 110, 217201, 2013.

S. -W. Chen, X. Lu, E. Blackburn, V. Lauter, H. Ambaye, K. T. Chan, E. E. Fullerton, A. E. Berkowitz and S. K. Sinha "Non-switchable Magnetic Moments in polycrystalline and (111)-epitaxial Permalloy/CoO Exchange-biased Bilayers", *Submitted*, 2013.

N. Eibagi, S. -W. Chen, H. Huo, J. Kan, V. Lauter, S. K. Sinha and E. E. Fullerton, "Interface Magnetization Study of Composite Bit Patterned Media", *in preparation*, 2014.

ABSTRACT OF THE DISSERTATION

X-ray and Neutron Scattering Studies of Magnetic Domain Dynamics and Spin Structures

by

San-Wen Chen

Doctor of Philosophy in Physics

University of California, San Diego, 2014

Professor Sunil Sinha, Chair

The study of magnetic spin structures at nanometer length scales and their dynamics is of both fundamental and technological importance. X-rays and neutrons are penetrating probes that are suitable for studying these in the bulk and the interfaces of the materials. In this thesis, the magnetic domain dynamics are studied by resonant soft x-ray scattering together with x-ray photon correlation spectroscopy. The domain fluctuations reveal when the temperature is close to the phase transition temperature. We find the domain wall dynamics in an antiferromagnet corresponds to a collective motion of spins and exhibit some universal features associated with the jamming behavior in many jammed soft condensed matter systems. We also discuss about the utilization of polarized neutron reflec-

tometry to study the interfacial spin structure in an exchange biased bilayer. The magnetization profiles are obtained which show that some spins are not completely reversible when the magnetic field is reversed. These spins include pinned uncompensated spins in the antiferromagnet and the interfacial spins exchange coupled to those spins. A previously established model was found to reproduce the magnetization profile observed. Finally, we carried out a grazing incidence small angle neutron scattering experiment on an optical grating as a way to test the Distorted Wave Born Approximation (DWBA). DWBA is briefly reviewed and we used it to calculate the scattering intensity of the system.

1 Introduction

The study of magnetism and magnetic materials is not only of fundamental importance but also practically very useful. From the scientific point of view, the spin structure in a magnetic system is an interplay between exchange energy, anisotropy, stray fields, magneto-elastic interactions and Zeeman energy etc. which provides a rich playground for studying a zoo of interactions. A composite material made of a magnetic material and a material with magnetic, electrical or elastic properties further opens up an infinite possibility for research and functionality. From the practical point of view, magnetism has been used extensively in the storage applications due to its non-volatile property and low-cost. The uses of magnetism include ID and credit cards, magnetic sweepers and hard disk drives in all personal computers. With the need for increasing density in the storage media, the size of the devices becomes smaller and comparable to the size of the domains. Also, in the composite materials, the key is to understand the interaction at the interfaces which happens on a nanometer length scale. Therefore, studying magnetism nowadays requires probes with high spatial resolution.

X-rays and neutrons are penetrating probes with wavelengths from about 0.1 nm to 10 nm, which are suitable for studying structures and dynamics of materials at nanometer length scales. Neutrons interact with nuclei in the material as well as electronic spins and therefore are suitable for studying both charge and magnetic structures. For x-rays, the magnetic cross section is generally very small compared to the charge cross section. However, the emergence of third-generation synchrotron radiation sources in recent years provides high-brilliance x-rays with tunable energy. This enables resonant magnetic scattering which involves tuning the x-ray energy to one of the magnetic resonance edges and the magnetic

scattering is enhanced dramatically. The strong penetrating power of x-rays and neutrons enable the study of the bulk properties, as well as looking at the interfaces of composite materials.

This work describes how we applied resonant x-ray and polarized neutron scattering to study the magnetic properties of several materials, including the domain dynamics in an antiferromagnet and magnetic nanostructures at an interface. The structure of this thesis is as follows: Chapter 2 includes a brief review of the scientific background of the techniques used in this work. The interaction between x-rays and matter, as well as resonant magnetic scattering (XRMS) will first be reviewed. Then the principle of x-ray photon correlation spectroscopy (XPCS) will be introduced which is useful for studying the slow dynamics of any disordered system. Polarized neutron reflectivity (PNR) is also included which can be used to study the spin structure of buried interfaces. Chapter 3 describes the study of domain wall dynamics in the helical antiferromagnet dysprosium. The magnetic domain wall fluctuations are related to the noise in the devices involving magnetic films. Detecting the domain fluctuations in an antiferromagnet is more difficult than in a ferromagnet because of zero net magnetic moment. With coherent x-rays, it is possible to look at the disorders in the systems such as domains. In this work, we combined resonant soft x-ray scattering and XPCS (with coherent x-rays) to study the domain fluctuations in dysprosium and we found that dynamics close to the phase transition temperature are similar to those in jammed soft matter systems. Chapter 4 presents the study of non-switchable moments in an exchange bias bilayer studied with polarized neutron reflectivity. Exchange bias occurs when a ferromagnet is coupled to an antiferromagnet. It is generally believed that some of the uncompensated antiferromagnetic spins are pinned at the interface which is responsible for the unidirectional anisotropy in the system. PNR was used to examine the magnetization depth profile in a permalloy/CoO exchange bias system subject to various magnetic fields. The results show that there are non-switchable spins at the interface which do not reverse completely when the field is reversed. A model which considers oxide nanoparticles forming at the interface was used to examine and explain the non-switchable magnetization

profile. Chapter 5 demonstrates the calculation of grazing-incidence small angle neutron scattering (GISANS) from a one dimensional optical grating. The Distorted Wave Born approximation (DWBA) is necessary for GISANS calculation and will be briefly reviewed. In Chapter 6, the main findings of the works are summarized and the future perspectives are briefly discussed.

2 Experimental Background

In this chapter, the experimental methods involved will be discussed. The antiferromagnetic domain wall dynamics experiment involves using resonant x-rays (section 2.1) to obtain enhanced magnetic scattering and x-ray photon correlation spectroscopy (section 2.2). Polarized neutron reflectivity was utilized in determining the interfacial spin structures which is discussed in section 2.3.

2.1 X-ray Interactions with Magnetic Materials

Electromagnetic waves interact with charge, as well as the magnetic moments of electrons in the materials. Usually the magnetic contribution is negligible compared to the charge contribution. However, when the x-ray energy is tuned to certain absorption edges of magnetic atoms/ions, the contribution of the magnetic scattering is greatly enhanced and can be comparable to that of charge scattering. This phenomenon is called resonant magnetic scattering and is widely used for studying magnetic materials nowadays. In this section, the interaction between x-rays and electronic charge will be briefly reviewed. Here we consider the photon-in-photon-out process and elastic scattering, the so called Thomson scattering (The energy transfer involved in x-ray inelastic scattering experiments is of the order of 1 eV and very difficult to resolve from a typical x-ray energy of the order of 1 keV). The principle of neutron scattering is very similar so the review is also very useful in discussing polarized neutron reflectivity which will be addressed in a later section. Then resonant x-ray magnetic scattering will be reviewed.

2.1.1 Charge Scattering

A portion of the following review is from the contents of the books by J. Als-Nielsen/D. McMorrow [1] and J. Daillant/A. Gibaud [2]. We start by considering an x-ray scattered by a single free electron. In the classical regime, the scattering event can be described as the electric field exerts a force on the electronic charge, which then accelerates the electron and radiates the scattering wave. Assuming the incident wave is a plane wave, the electron vibrates in the electric field direction and acts like a small dipole antenna. The radiated wave depends on the polarization of the incident beam, and in the far-field limit, the radiated electric field (modulus squared) at a distance R can be expressed as,

$$|E_{rad}|^2 = (\frac{r_0^2}{R^2})\langle E_0^2\rangle P \tag{2.1}$$

where r_0 is known as the Thomson scattering length, or the classical electron radius, which represents the ability of an electron to scatter the x-ray,

$$r_0 = \frac{e^2}{4\pi\epsilon_0 mc^2} = 2.81794 \times 10^{-15}\text{m} \tag{2.2}$$

P is the polarization factor which depends on the incident x-ray polarization. For a synchrotron source, the electrons orbit in a horizontal plane which generates a linearly, horizontally polarized x-ray, and P is:

$$P = \begin{cases} 1 & \text{vertical scattering plane} \\ \cos^2\phi & \text{horizontal scattering plane} \end{cases} \tag{2.3}$$

where ϕ is the scattered angle out of the scattering plane. For an unpolarized x-ray source such as a tube machine, the polarization factor is $(1+\cos^2\phi)/2$.

In the experiments, the detectors measure the scattered intensity by detecting single photon events. The scattered intensity I_{SC} is proportional to $|\mathbf{E}_{rad}|^2$. Often we normalize the scattered intensity by the incident flux and this lead to the definition of the differential cross section:

$$(\frac{\mathrm{d}\sigma}{\mathrm{d}\Omega}) \equiv \frac{I_{SC}}{(I_0/A_0)\Delta\Omega} = \frac{|\mathbf{E}_{rad}|^2 R^2}{|\mathbf{E}_{in}|^2} \tag{2.4}$$

where $\Delta\Omega$ is the solid angle of the detector. Insertion of equation (1) into equation (4) yields the differential cross section for Thomson scattering:

$$(\frac{\mathrm{d}\sigma}{\mathrm{d}\Omega}) = r_0^2 P \tag{2.5}$$

Now we consider the scattering by an atom with Z electrons. The electron distribution is represented by the number density $\rho(\mathbf{r})$. The scattered radiation field is given by the superposition of the scattering from the whole volume. The scattering from any two locations with a displacement vector $\mathbf{r}$ has a phase difference of

$$\Delta\phi(\mathbf{r}) = (\mathbf{k}_f - \mathbf{k}_0) \cdot \mathbf{r} = \mathbf{Q} \cdot \mathbf{r} \tag{2.6}$$

where $\mathbf{k}_0$ is the incident wavevector and $\mathbf{k}_f$ is the outgoing wavevector. $\mathbf{Q}$ is the momentum transfer of the process and is called the wavevector transfer or the scattering vector. Thus the total scattering length from the atom is simply the Fourier transform of the electron density $\rho(\mathbf{r})$

$$r_0 f^0(\mathbf{Q}) = r_0 \int \rho(\mathbf{r}) e^{i\mathbf{Q}\cdot\mathbf{r}} \mathrm{d}\mathbf{r} \tag{2.7}$$

where $f^0(\mathbf{Q})$ is known as the atomic form factor. In the limit of forward scattering, $Q \to 0$, all the scattering elements are in-phase and yield $f^0(\mathbf{Q} = 0) = Z$, the total number of electrons in the atom. The scattering from the atom is of course a quantum mechanical effect. The electrons at different energy levels in the atom respond to x-ray photons differently, which will lead to a decrease of the total scattering length. A dispersive term in the form factor is therefore necessary. Together with an absorption term, the atomic form factor is now

$$f(\mathbf{Q}, \omega) = f^0(\mathbf{Q}) + f'(\omega) + if''(\omega) \tag{2.8}$$

where $\hbar\omega$ represents the incident beam energy.

The refractive index of a material describes the phase speed of an electromagnetic wave in the medium. For non-magnetic materials, assuming the frequency of the radiation is much higher than the resonant frequency of the atoms,

ω_j, which is generally true in the x-ray regime, the refractive index is slightly smaller than 1 and can be written as:

$$n(\mathbf{r},\omega) = 1 - \delta(\mathbf{r},\omega) + i\beta(\mathbf{r},\omega) \tag{2.9}$$

with dispersion and absorption terms

$$\delta(\mathbf{r},\omega) = \frac{2\pi r_0}{k^2}\sum_j \rho_j(\mathbf{r})\{f_j^0(\mathbf{Q}) + f_j'(\omega)\} \tag{2.10}$$

$$\beta(\mathbf{r},\omega) = \frac{2\pi r_0}{k^2}\sum_j \rho_j(\mathbf{r}) f_j''(\omega) \tag{2.11}$$

where ρ_j is the atomic number density of atom j. In general, the atoms in the materials have fluctuations and a multiplication of a Debye-Waller factor is needed in the above expressions. If the medium is macroscopically homogeneous, the electron density is a constant. The refractive index is approximately

$$n \approx 1 - \frac{2\pi r_0 \rho}{k^2} + i\frac{\mu}{2k} \tag{2.12}$$

where μ is the linear absorption coefficient. For widely used Cu K_α x-ray sources (E = 8.04 keV), δ is typically $\sim 10^{-6}$ and β is one to three orders of magnitude smaller.

2.1.2 Magnetic Scattering

Electromagnetic waves also interact with the electronic spins in the materials via relativistic effects. The coherent elastic scattering amplitude for non-resonant x-ray scattering is given by [3, 4, 5, 6]

$$f^{mag} = ir_0(\hbar\omega/mc^2) f_D \left[\frac{1}{2}\mathbf{L}(K)\cdot\mathbf{A} + \mathbf{S}(K)\cdot\mathbf{B}\right] \tag{2.13}$$

where $\mathbf{L}(K)$ and $\mathbf{S}(K)$ are the atomic orbital and spin magnetization densities respectively. $\mathbf{A}$ and $\mathbf{B}$ are the polarization vectors determined by $\mathbf{k}_0$, $\mathbf{e}_0$, $\mathbf{k}_f$, $\mathbf{e}_f$, and f_D is the Debye-Waller factor. Now the total atomic form factor is $f \approx f^0 + f' + if'' + f^{mag}$. The non-resonant magnetic scattering is thus considerably weaker than the charge scattering. Consider Cu K_α x-ray at an energy of 8.04 keV, the $(\hbar\omega/mc^2)$ factor is ~ 0.016.

When investigating the magnetic spiral structure of holmium crystal, Gibbs et al. [7] observed an enhancement of the magnetic scattering (by a factor of 50) when the synchrotron x-ray energy was tuned to the L_{III} absorption edge, as well as a complex polarization dependence. It was realized that an enhancement of magnetic scattering occurs when involving a low order electric multipole transition, e.g. dipole or quadrupole, between a core atomic level and an unfilled atomic shell, or narrow band. In the holmium case, it involves a quadrupole transition from $2p \rightarrow 4f$ and a dipole transition from $2p \rightarrow 5d$. The exclusion principle allows transitions only to unoccupied states which results in the sensitivity to the magnetization of the f and d bands.

The contribution to the scattering amplitude from an electric 2^L-pole resonance (EL) is given by [8, 9]

$$f_{EL}^{xres}(\mathbf{k}_f, \mathbf{e}_f; \mathbf{k}_0, \mathbf{e}_0) = \frac{4\pi}{|k|} f_D \sum_{M=-L}^{L} \left[\mathbf{e}_f^* \cdot \mathbf{Y}_{LM}^{(e)}(\hat{\mathbf{k}}_f) \mathbf{Y}_{LM}^{(e)*}(\hat{\mathbf{k}}_0) \cdot \mathbf{e}_0 \right] F_{LM}^{(e)}(\omega) \quad (2.14)$$

where $\mathbf{Y}_{LM}^{(e)}$ are the vector spherical harmonics. $F_{LM}^{(e)}(\omega)$ is the transition matrix element and is determined by the occupation and the distribution of the initial and final states

$$F_{LM}^{(e)}(\omega) = \sum_{\alpha,\eta} \left[\frac{p_\alpha p_\alpha(\eta) \Gamma_x(\alpha M \eta; EL)/\Gamma(\eta)}{x(\alpha, \eta) - i} \right] \quad (2.15)$$

p_α is the probability for the ion to have the initial ground state $|\alpha\rangle$. $|\eta\rangle$ is the excited state with one electron being excited to unoccupied levels and leaving a hole at the core level. $p_\alpha(\eta)$ is basically the probability of the state being vacant for the transition from $|\alpha\rangle$. Γ_x gives the partial width for EL radiative decay from $|\eta\rangle$ to $|\alpha\rangle$ and $\Gamma(\eta)$ is the total width for the excited state $|\eta\rangle$. In the denominator, $x(\alpha, \eta) = (E_\eta - E_\alpha - \hbar\omega)/(\Gamma(\eta)/2)$ is the deviation from resonance in units of $\Gamma(\eta)/2$. The divergence when the photon energy equals $(E_\eta - E_\alpha)$ causes the large enhancement of the scattering amplitude.

In the case of studying the spiral magnetic structure in dysprosium, as will be later discussed in Chapter 3, we exploited resonant x-rays in the soft x-ray energy range. The energy of a soft x-ray photon typically ranges from a few

hundred eVs to a few keV, which is at the M-edge for rare earth elements. The M-edge transition from $3d \rightarrow 4f$ is magnetically sensitive and dominated by the electric dipole (E1) transition. For the E1 transition, we have

$$\left[\mathbf{e}_f^* \cdot \mathbf{Y}_{1\pm1}^{(e)}(\hat{\mathbf{k}}_f)\mathbf{Y}_{1\pm1}^{(e)*}(\hat{\mathbf{k}}_0) \cdot \mathbf{e}_0\right] = \left(\frac{3}{16\pi}\right)\left[\mathbf{e}_f^* \cdot \mathbf{e}_0 \mp i(\mathbf{e}_f^* \times \mathbf{e}_0) \cdot \hat{\mathbf{z}} - (\mathbf{e}_f^* \cdot \hat{\mathbf{z}})(\mathbf{e}_0 \cdot \hat{\mathbf{z}})\right] \quad (2.16a)$$

$$\left[\mathbf{e}_f^* \cdot \mathbf{Y}_{10}^{(e)}(\hat{\mathbf{k}}_f)\mathbf{Y}_{10}^{(e)*}(\hat{\mathbf{k}}_0) \cdot \mathbf{e}_0\right] = \left(\frac{3}{8\pi}\right)(\mathbf{e}_f^* \cdot \hat{\mathbf{z}})(\mathbf{e}_0 \cdot \hat{\mathbf{z}}) \quad (2.16b)$$

$\hat{\mathbf{z}}$ is the unit magnetization vector. Thus we obtain the scattering amplitude for dipole transition

$$f_{E1}^{xres} = \frac{3}{4|k|}\Big\{(\mathbf{e}_f^* \cdot \mathbf{e}_0)[f_{11}^{(e)} + F_{1-1}^{(e)}] - i(\mathbf{e}_f^* \times \mathbf{e}_0) \cdot \hat{\mathbf{z}}[F_{11}^{(e)} - F_{1-1}^{(e)}] + (\mathbf{e}_f^* \cdot \hat{\mathbf{z}})(\mathbf{e}_0 \cdot \hat{\mathbf{z}})[2F_{10}^{(e)} - F_{11}^{(e)} - F_{1-1}^{(e)}]\Big\} \quad (2.17)$$

The first term $(\mathbf{e}_f^* \cdot \mathbf{e}_0)$ is independent of the direction of the magnetic moment and represents a resonance modification of charge scattering. The second term $i(\mathbf{e}_f^* \times \mathbf{e}_0) \cdot \hat{\mathbf{z}}$ depends linearly on the direction of the magnetic moment and gives rise to first harmonic satellites in an antiferromagnet. When using linearly polarized light (σ or π polarization which is perpendicular or parallel to the scattering plane respectively), incident σ light will only be scattered to π and vice versa. We used linear polarized light from the synchrotron to reach the first satellite peak from the spiral antiferromagnetic structure, so this linear term is dominant. The third term $(\mathbf{e}_f^* \cdot \hat{\mathbf{z}})(\mathbf{e}_0 \cdot \hat{\mathbf{z}})$ is quadratically dependent of $\hat{\mathbf{z}}$ and will give rise the second harmonic satellite. In the case of M_{IV} or M_V edges in dysprosium, the very strong E1 transition to a $4f$ orbital can give rise to a resonant magnetic scattering amplitude on the order of $100r_0$!

2.2 X-ray Photon Correlation Spectroscopy

To obtain coherent x-rays is relatively difficult compared to visible light because of their small wavelengths and lack of monochromaticity. However, in the last two decades, due to the invention of the bright third-generation synchrotron

sources, a partially coherent beam of x-ray photons can be obtained and the advantages of utilizing the coherent properties of x-rays has emerged. In the last decade, the free electron laser (FEL) which is based on the principle of self-amplified stimulated emission (SASE) and which produce completely coherent x-ray pulses was achieved [10]. Currently, performing experiments with coherent x-rays is a rapidly growing research field. Coherent x-ray can be used to study the exact static structure with phase retrieval and speckle reconstruction methods. It can also be used to study the dynamics of a system through the technique known as x-ray photon correlation spectroscopy (XPCS), which is the focus of this section.

2.2.1 Coherence and Speckles

The coherent properties of light have been known for hundreds of years. The famous Young's double slits experiment in the early 1800's was a perfect demonstration of the interference effect from the coherent light. The invention of the laser further enormously expanded the field and coherent light was used to study the exact structure and dynamics of many systems. X-rays have smaller wavelengths and thus can resolve much finer structures. However, obtaining coherent x-rays is more difficult.

So far we simplified our discussion assuming that the x-ray beam is a perfect plane wave. A real beam deviates from a plane waves in two ways: First, the beam is not monochromatic. Thus a x-ray beam of different wavelengths will be completely out of phase after travelling a certain distance. Second, the beam does not travel in a well-defined direction. This happens when the size of the beam is finite. The coherence lengths of the x-ray beam is thus related to these two properties [1]

$$\begin{aligned} \xi_l &= \frac{1}{2}\frac{\lambda^2}{\Delta\lambda} \\ \xi_t &= \frac{\lambda}{2}\left(\frac{R}{\sigma_t}\right) \end{aligned} \tag{2.18}$$

where ξ_l is the longitudinal coherence length and ξ_t is the transverse coherence length. R is the distance from the x-ray source to the measuring point and σ_t is the lateral size of the source. Thus the coherence volume is proportional to λ^4,

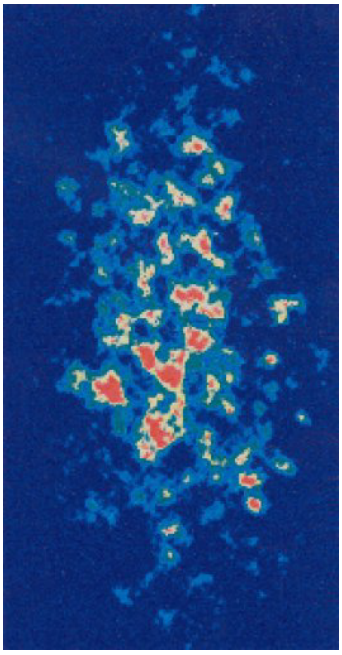

Figure 2.1: First observed x-ray speckle pattern of the (100) disordered superlattice peak of Cu_3Au [11].

which makes the coherent volume of x-rays ten to twelve orders of magnitude lower than that of the visible light. For third-generation synchrotrons, the vertical size of the beam is $\sim$ 100 μm and the distance from source to sample can be $\sim$ 10 m. Thus for a 1 nm wavelength soft x-ray, ξ_t is about 50 μm. The longitudinal coherence length $\xi_l \sim 5\mu m$ assuming $\Delta\lambda/\lambda = 10^{-4}$.

The coherent intensity (i.e. the intensity of coherent photons per unit time through a pinhole of dimension $\xi_x\xi_y$) also depends on the brightness (number of photons per unit area per unit solid angle) of the beam:

$$I_{coh} = \frac{B\sigma_x\sigma_y\xi_x\xi_y}{R^2} = \frac{\lambda^2 B}{4} \tag{2.19}$$

where B is the brightness of the source. The third-generation synchrotrons produce high intensity and well-collimated x-ray beams which imply very high brightness. This makes coherent x-ray scattering possible by using a small aperture to transmit mainly the coherent fraction of the beam. In other words, we can sacrifice the x-ray intensity and obtain a partially coherent beam.

In the kinematic approximation, the scattering from a sample is the Fourier transform of its electron density and the differential cross section is

$$\frac{\mathrm{d}\sigma}{\mathrm{d}\Omega}(\mathbf{Q}) = r_0^2 P \int\int \mathrm{d}\mathbf{r}\mathrm{d}\mathbf{r}' \langle \rho(\mathbf{r})\rho(\mathbf{r}')\rangle_t e^{-i\mathbf{Q}\cdot(\mathbf{r}-\mathbf{r}')} \tag{2.20}$$

where the average is over the time span for detection. Consider a coherent beam incident on a sample with some static random disorder, then the scattering from a sample point will have some phase difference from the scattering from another point. The electric field scattered from the sample will superimpose coherently and gives rise to an interference pattern which corresponds to the exact configuration of the sample. This is the so called speckle pattern which is a unique fingerprint of the sample. Any fluctuation in the sample will cause a change in the speckle pattern. Even with the third-generation synchrotron, obtaining speckle patterns can still be a difficult job because the coherent volume must be significantly larger than the length scale of the random fluctuation in the sample, i.e. the instrumental resolution must be good enough to resolve the speckles. Theoretical treatment for scattering from a partially coherent beam is therefore very complicated [12, 13, 14, 15]. The first reported x-ray speckle pattern was obtained from a (100) disordered superlattice peak of Cu_3Au (Figure 2.1) [11]. Since then speckle patterns have been observed in many systems such as aerogels [16], charge density waves in Cr [17] and magnetic systems [18, 19].

2.2.2 Photon Correlation Spectroscopy

As mentioned in the last section, a speckle pattern is the Fourier representation of the random disorder in the sample. Any fluctuation in the sample will cause a fluctuation in the speckle pattern as well. The time-dependent variation of the speckles in reciprocal space vector $\mathbf{Q}$ corresponds to the dynamical properties at the corresponding length scale $2\pi/|\mathbf{Q}|$. This is the principle of photon correlation spectroscopy (PCS). PCS with visible light is known as dynamical light scattering (DLS) and is a widely used technique [21, 22, 23]. XPCS is the extension of DLS and can resolve dynamics at much smaller length scales. XPCS can also measure dynamics at long time scales (milli-seconds to hours) and is a complementary

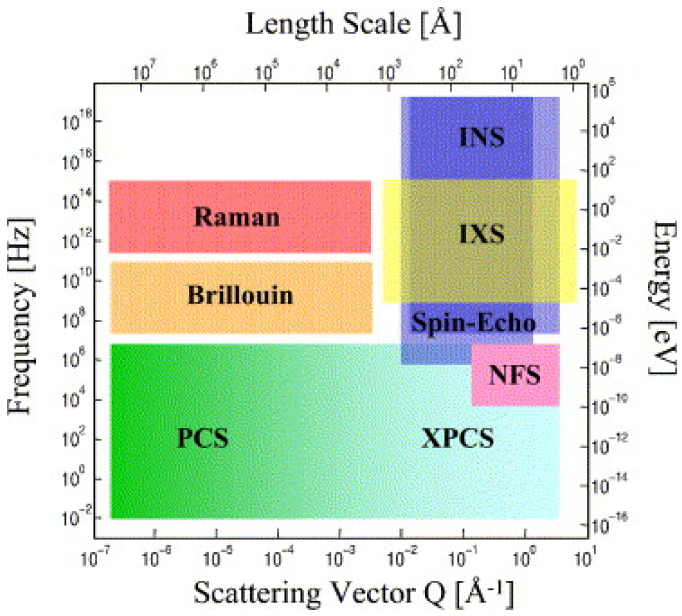

Figure 2.2: Time-scale (or frequency) and the scattering vector covered by the x-ray photon correlation spectroscopy and various complimentary techniques [20].

technique to neutron spin echo (See Figure 2.2). Compared to visible light, x-rays usually have weaker interaction with matter and thus the multiple scattering problem is minimized, which makes XPCS analysis less complicated than DLS.

The most common measuring mode with XPCS is the homodyne method, which only measures the scattered intensity and calculates the correlation function. On the contrary, the heterodyne mode measures the interference between a reference beam and the scattered beam which is sometime used when the beam for total reflection or Bragg reflection is strong enough to serve as a reference beam [24, 25]. Here we focus on the homodyne mode used in our experiments. The intensity-intensity correlation function is written as

$$g_2(\mathbf{Q},\tau) = \frac{\langle I(\mathbf{Q},t)I(\mathbf{Q},t+\tau)\rangle_t}{\langle I(\mathbf{Q},t)\rangle_t^2} \tag{2.21}$$

where $\langle ...\rangle_t$ is an over all measuring time. The intensity $I(\mathbf{Q},t)$ of the scattered beam is proportional to the Fourier transform of particle density correlation function: $I(\mathbf{Q},t) \propto \langle \rho(\mathbf{Q},t)\rho^*(\mathbf{Q},t)\rangle$. Assuming the scattered electric fields are random Gaussian variables, the intensity-intensity autocorrelation function (second order

correlation) is related to the first order correlation function by the Siegert relation [21]

$$g_2(\mathbf{Q},\tau) = 1 + |g_1(\mathbf{Q},\tau)|^2 \tag{2.22}$$

where

$$g_1(\mathbf{Q},\tau) = \frac{\langle E(\mathbf{Q},t)E^*(\mathbf{Q},t+\tau)\rangle_t}{\langle I(\mathbf{Q},t)\rangle_t} \tag{2.23}$$

The derivation of this equation assumes perfect coherence. In reality, the illuminated sample volume is usually larger than the coherence volume. Also, due to the finite acceptance of the detector, the resolution function has to be considered. g_2 is therefore usually written as

$$g_2(\mathbf{Q},\tau) = 1 + \beta(\mathbf{Q})|f(\mathbf{Q},\tau)|^2 \tag{2.24}$$

Here β is the contrast parameter, which depends on the coherent volume and the illuminated sample volume. β is also related to the source properties and the acceptance angle of the detectors [26, 27]. In the ideal case, $\beta = 1$. In actual XPCS experiment, because of the partial coherence of the beam and other instrumental imperfections, $\beta \ll 1$. Since it is a sample-independent parameter, it is usually treated as a fitting parameter and normalized out during data analysis. $f(\mathbf{Q},\tau)$ is the normalized intermediate scattering function defined as $g_1(\mathbf{Q},\tau)/g_1(\mathbf{Q},0)$, with

$$g_1(\mathbf{Q},\tau) = \int\int d\mathbf{r}d\mathbf{r}' e^{-i\mathbf{Q}\cdot(\mathbf{r}-\mathbf{r}')}\langle\rho(\mathbf{r},0)\rho(\mathbf{r}',\tau)\rangle \tag{2.25}$$

$$\text{and} \quad g_1(\mathbf{Q},0) = \int\int d\mathbf{r}d\mathbf{r}' e^{-i\mathbf{Q}\cdot(\mathbf{r}-\mathbf{r}')}\langle\rho(\mathbf{r},0)\rho(\mathbf{r}',0)\rangle \tag{2.26}$$

Typical systems investigated by XPCS include metal colloids in glycerol [28, 29], binary alloys [30], melted polymer films [31, 32], liquid surfaces [24] and binary fluid [25] etc. For the surface sensitive XPCS, the density in the intermediate scattering function is described by the electron density at the sample surface, which is related to the surface height-height correlation function. More recently, XPCS is extended to more solid state systems including charge density wave [17], antiferromagnetic domains [18, 19] etc.

In XPCS experiments, either a point detector or an area detector, such as charge coupled device (CCD) [33] or Pilatus detector, can be utilized to measure

the scattered intensity. A point detector can in principle measure faster dynamics compared to using an area detector because of its faster rate. However, the area detector in general has a better signal to noise ratio (SNR). The SNR in XPCS using a CCD detector can be expressed as [34]

$$SNR_{CCD} = \beta i \eta \sqrt{T\tau_\alpha}\sqrt{\tau_\alpha F}\sqrt{n_p} \tag{2.27}$$

where β is the speckle contrast, η is the detector efficiency, i is the mean count rate, T is the total measuring time, τ_α is the accumulation time, F is the frame rate and n_p is the number of pixels. In comparison, for an ideally efficient point detector, $SNR_1 = \beta i\sqrt{T/F}$. Thus

$$\frac{SNR_{CCD}}{SNR_1} = \eta\tau_\alpha F\sqrt{n_p} \tag{2.28}$$

Usually the efficiency of a CCD is ~ 0.5 and the number of pixels corresponding to a $|\mathbf{Q}|$ on a CCD detector is $\sim 10^4$, which yields a 50 times better SNR compared to a point detector.

A point detector can in principle measure faster dynamics because of its faster "frame rate". When the dynamics are ergodic, the time ensemble average is the same as the spatial ensemble average. Therefore, using a point detector can yield the same result as using an area detector. The measuring time must be much longer than the time scale of the dynamics to get good statistics. The use of a CCD detector shortens the measuring time by measuring multiple speckles at the same $\mathbf{Q}$. Each pixel on the CCD serves as an individual point detector and one can calculate the autocorrelation function on each pixel then take an average. This is the so-called multi-speckle method [35]. With the multi-speckle method, the measuring time only needs to be comparable to the time scale of the system dynamics and one can get the contrast at the same time. Therefore the method can also be used to study non-ergodic systems, such as jammed and glassy systems [36].

2.3 Polarized Neutron Reflectivity

Reflectometry involves the measurement of the reflected intensity of electromagnetic waves or neutrons reflected from flat surfaces or interfaces. In the case

of specular reflectivity where the reflected angle α_f equals the incident angle α_i, one gets the in-plane averaged density profile along the surface normal to an unprecedented precision. While x-rays are sensitive to the change of refractive index of the material which is related to the electron density, neutrons are sensitive to the profile of density of the nuclei. More importantly, a neutron has a spin which interacts with the unpaired electronic spins so that neutron reflectometry can also be used to measure the magnetization density profile. In this section we briefly review the principle of polarized neutron reflectivity which we used to study the magnetization in an exchange bias system.

2.3.1 Refractive Index

In Figure 2.3, we show the geometry of a typical reflectometry measurement and define the scattering vector directions. Similar to x-rays scattered by fixed electrons discussed in section 2.1, the scattering strength of neutrons being scattered by a fixed nucleus can be characterized by a scattering length b [37]. Neutron reflectometry involves measurements that are in a fairly small Q_z range, and the scattering medium can be considered as possessing a continuous scattering length density defined as the density of the scattering centers N multiplied the coherent neutron scattering length b of the species:

$$\rho = \sum_{i=1}^{N} N_i b_i \tag{2.29}$$

The nuclear scattering length density of materials can be found in various sources [38, 39].

The reflectivity is defined as the reflected intensity from the flat surface normalized by the incident intensity. For neutrons we can solve the time-independent Schrödinger equation:

$$\left[\frac{\hbar^2}{2m_n}\frac{\partial^2}{\partial z^2} + V(z)\right]\Psi(z) = E\Psi(z) \tag{2.30}$$

with scattering potential

$$V(z) = \frac{2\pi\hbar^2}{m_n}\rho(z) \tag{2.31}$$

Consider a neutron beam incident on a surface from vacuum, where the initial energy of the neutron is $\hbar^2 k_0^2/2m_n$. Here we only consider the elastic scattering and equation (2.30) can be written as

$$\left[\frac{\partial^2}{\partial z^2} + k_0^2 - 4\pi\rho(z)\right]\Psi(z) = 0 \tag{2.32}$$

Thus the wavevector in the medium can be written as

$$k_1 = n_1 k_0 = \sqrt{1 - \frac{4\pi\rho}{k_0^2}}k_0 \tag{2.33}$$

where n_1 is the refractive index of the medium. Neutron reflectometry usually utilizes the time-of-flight technique. With a continuous wavelength spectrum of neutrons, a range of $R(Q_z)$ can be measured simultaneously with a fixed incident angle. Note that when the wavelength is greater than $\sqrt{\pi/\rho}$, k_1 is purely imaginary which leads to an evanescent wave in the medium and total external reflection at small Q_z.

2.3.2 Reflectometry with Unpolarized Neutrons

To determine the reflectivity $R(Q_z)$, we need to calculate the probability of the neutron being reflected or transmitted by the sample surface. To achieve that, we need to solve the Schrödinger equation shown in equation (2.30), with the fact that the particle numbers and the transverse momentum is conserved at the interface. Consider a single flat surface which is perfectly smooth at $z = 0$, below which is a medium with refractive index n_1 extended to infinity, the wave function can be written as

$$\Psi(z) = \begin{cases} e^{ik_0 z} + re^{-ik_0 z} & \text{z} > 0 \\ te^{ik_1 z} & \text{z} < 0 \end{cases} \tag{2.34}$$

where r is the reflection coefficient and t is the transmission coefficient. The boundary condition at $z = 0$ is

$$\begin{pmatrix} 1 + r \\ ik_0(1 - r) \end{pmatrix} = \begin{pmatrix} t \\ ik_1 t \end{pmatrix} \tag{2.35}$$

Solving equation (2.35) gives the reflection coefficient r

$$r = \frac{k_0 - k_1}{k_0 + k_1} \tag{2.36}$$

and the reflectivity from a single flat surface with no roughness is

$$R = |r|^2 = \left|\frac{k_0 - k_1}{k_0 + k_1}\right|^2 = \left|\frac{1 - n_1}{1 + n_1}\right|^2 \tag{2.37}$$

This is the Fresnel reflectivity [40]. In the large Q_z regime, the kinematic theory, or Born approximation,

$$R_{BA} \propto \frac{1}{Q_z^2}\left|\int_{-\infty}^{+\infty} \rho(z) e^{iQ_z z} dz\right|^2 \tag{2.38}$$

matches the dynamical theory results very well and yields the $R_{BA} \sim Q_z^{-4}$, the so called Porod's law [41].

Now consider the case of a thin slab of n_1 with thickness Δ on top of a substrate n_2, the boundary condition equations can be written as

$$\begin{pmatrix} \cos(k_1\Delta) & \frac{1}{k_1}\sin(k_1\Delta) \\ -k_1\sin(k_1\Delta) & \cos(k_1\Delta) \end{pmatrix} \begin{pmatrix} 1 + r \\ ik_0(1 - r) \end{pmatrix} = \begin{pmatrix} t \\ ik_2 t \end{pmatrix} e^{1k_2\Delta} \tag{2.39}$$

Solving equation (2.39) yields the reflection coefficient

$$r_{0,1} = \frac{r'_{0,1} + r'_{1,2}e^{ik_1 2\Delta}}{1 + r'_{0,1}r'_{1,2}e^{ik_1 2\Delta}}, \quad \text{with} \quad r'_{m,n} = \frac{k_m - k_n}{k_m + k_n} \tag{2.40}$$

Note that $r_{1,2} = r'_{1,2}$ because there is no reflection in the substrate. The above equation can be generalized to any number of flat thin slabs on a substrate.

$$r_{n-1,n} = \frac{r'_{n-1,n} + r_{n,n+1}e^{iQ_{z,n}\Delta_n}}{1 + r'_{n-1,n}r_{n,n+1}e^{iQ_{z,n}\Delta_n}} \tag{2.41}$$

Utilizing the fact that there is no reflection below the substrate, the reflection coefficient of the last interface $r_{N,\infty}$ is identical to the Fresnel reflection coefficient $r'_{N,\infty}$. $r_{N,\infty}$ can therefore be brought into the equation to solve $r_{N-1,N}$, then using it iteratively to solve the reflection from the surface $r_{0,1}$. This is the principle of the Parratt formalism [42] and is a fully dynamical theory to calculate the reflection coefficients.

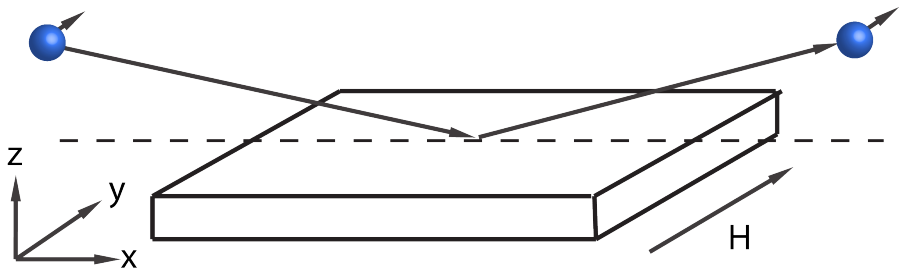

Figure 2.3: Schematic of the neutron reflectometry geometry with an applied magnetic field.

In real-world stratified media, there is roughness between layers instead of sharp interfaces. We usually use an error function to simulate the gradual change of density across the interface between the two media.

$$\rho(z) = \rho_1 + \frac{\rho_2 - \rho_1}{2}\left[1 + erf(\frac{z - z_0}{\sqrt{2}\sigma})\right] \tag{2.42}$$

where z_0 is the center of the interface and σ is a parameter representing the root mean square roughness. The larger the roughness, the more gradually the density changes. With this expression for density, we can utilize the Parratt iterative formalism to calculate the reflectivity for almost all stratified media with a reasonable roughness. We use equation (2.42) to express $\rho(z)$ of the sample and divide it into small slices with constant densities. The thinner the slabs, the better it simulates the real density profile. A guide for determining the number of slices is to use the sample thickness in Angstroms because the wavelength of x-rays or neutrons is at the level of Angstroms, and therefore the depth resolution is also at the same level. Neutron reflectivity has been discussed in the literature [43, 44, 45, 46, 47].

2.3.3 Reflectometry with Polarized Neutrons

Now we consider a polarized neutron scattered by a magnetized sample, as shown in Figure 2.3. The scattering potential is from both nuclear and magnetic interactions and involves two neutron scattering lengths b^+ and b^-, corresponding to neutron spins parallel or anti-parallel to the magnetization of the sample. The

scattering potential is given by

$$V = V_n + V_m = V_n \mp \boldsymbol{\mu} \cdot \mathbf{B} \tag{2.43}$$

where $\mathbf{B} = \mathbf{H} + \mu_0\mathbf{M}$ is the magnetic induction. $\boldsymbol{\mu} = \mu_n\boldsymbol{\sigma}$ with $\mu_n = -1.913\mu_N$ and σ is a linear combination of the 2×2 Pauli matrices [48]. Thus B is a 2×2 matrix operating on a spinor state of neutron spin up or down. Since the external magnetic field is the same across all interfaces, the difference of the scattering potential across the interfaces is only related to the magnetization difference and the scattering potential can be written in the following matrix form:

$$\delta V(z) = \frac{2\pi\hbar^2}{m_n}\begin{pmatrix}\rho_n & 0\\ 0 & \rho_n\end{pmatrix} \mp \mu_n \begin{pmatrix} M_y & M_x - iM_z \\ M_x + iM_z & M_y\end{pmatrix} \tag{2.44}$$

The magnetic scattering length density is defined as

$$\boldsymbol{\rho}_m = -\frac{m_n}{2\pi\hbar^2}\mu_n\mathbf{M} = C\mathbf{M} \tag{2.45}$$

with constant $C = 2.853 \times 10^{-9}\mathring{A}^{-2}cm^3/emu$ [ref]. The scattering potential can be then written in a concise form:

$$\begin{aligned}\delta V(z) &= \tfrac{2\pi\hbar^2}{m_n}\begin{pmatrix}\rho_{++} & \rho_{+-}\\ \rho_{-+} & \rho_{--}\end{pmatrix} \\ &= \tfrac{2\pi\hbar^2}{m_n}\begin{pmatrix}\rho_n + \rho_{my} & \rho_{mx} - i\rho_{mz}\\ \rho_{mx} + i\rho_{mz} & \rho_n - \rho_{my}\end{pmatrix}\end{aligned} \tag{2.46}$$

The four states ρ_{++}, ρ_{+-}, ρ_{-+} and ρ_{--} corresponds to spin up (+) or spin down (-) neutrons being scattered into spin up (+) or spin down (-) states. Since reflectivity only measures the component perpendicular to Q_z, the spin-flip component $\rho_{+-} = \rho_{-+} = \rho_{mx}$. And the wavevector of a neutron becomes birefringent in a magnetic field,

$$k_\pm = n_\pm k_0 = \sqrt{1 - \frac{4\pi(\rho_n \pm |\boldsymbol{\rho}_m|)}{k_0^2}}k_0 \tag{2.47}$$

In many cases, the neutrons are either polarized parallel or antiparallel to the sample magnetization. In these cases, the Parratt formalism can still be used to calculate the R^{++} and R^{--} with a spin-dependent scattering length density. In

other cases, the above constraint is not necessarily true. For an example, when the material has a strong uniaxial anisotropy so that the magnetization could be oriented with an angle with the applied field, or the spins form a partial domain walls along the surface normal direction. In such cases, the full polarization analysis including the spin-flip channel is necessary, and the matrix formalism is discussed in the literature [49, 50, 51, 52].

Neutron reflectometry measures the layer thickness with very high accuracy. A film with thickness Δ will result in Kiessig fringes in the reflectivity curve with a period of $\Delta Q_z = 2\pi/\Delta$, which is ideally the Q_z range for resolving the thickness of the film. A small change of the film thickness is resolvable if the change in Q_z is larger than the Q_z resolution of the reflectometer. For a time-of-flight neutron reflectometer, the resolution effect mainly comes from the divergence angle and the monochromaticity:

$$\left(\frac{\delta Q_z}{Q_z}\right)^2 \approx \left(\frac{\delta\theta}{\theta}\right)^2 + \left(\frac{\delta\lambda}{\lambda}\right)^2 \tag{2.48}$$

A typical angular resolution $\delta\theta/\theta$ is of order 2% and the wavelength resolution is usually smaller than 1%. So the resolution in Q_z is typically smaller than 3%. For a 10 nm-thick film, one can easily resolve a thickness change of few Angstroms. This is the reason one can rely on the polarized neutron reflectometry to resolve very subtle change of spin structures at the interfaces. The resolution effect needs to be taken into account in the reflectivity calculation results in a smearing of the fringes in the curves.

Bibliography

[1] J. Als-Nielsen and D. McMorrow. *Elements of Modern X-ray Physics*. Wiley, 2011.

[2] J. Daillant and A. Gibaud. *X-ray and neutron reflectivity: principles and applications*. Springer, 2009.

[3] M. Blume. Magnetic scattering of x rays (invited). *Journal of Applied Physics*, 57(8):3615–3618, 1985.

[4] S. W. Lovesey. Magnetic photon scattering. *Journal of Physics C: Solid State Physics*, 20(34):5625, 1987.

[5] P. M. Platzman and N. Tzoar. Magnetic scattering of x rays from electrons in molecules and solids. *Phys. Rev. B*, 2:3556–3559, 1970.

[6] M. Blume and D. Gibbs. Polarization dependence of magnetic x-ray scattering. *Phys. Rev. B*, 37:1779–1789, 1988.

[7] D. Gibbs, D. R. Harshman, E. D. Isaacs, D. B. McWhan, D. Mills, and C. Vettier. Polarization and resonance properties of magnetic x-ray scattering in holmium. *Phys. Rev. Lett.*, 61:1241–1244, 1988.

[8] J. P. Hannon, G. T. Trammell, M. Blume, and D. Gibbs. X-Ray Resonance Exchange Scattering. *Phys. Rev. Lett.*, 61(10):1245–1248, 1988.

[9] J. P. Hannon and G. T. Trammell. Mössbauer diffraction. ii. dynamical theory of mössbauer optics. *Phys. Rev.*, 186:306–325, 1969.

[10] B. W. J. McNeil and N. R. Thompson. X-ray free-electron lasers. *Nature Photonics*, 4(12):814–821, 2010.

[11] M. Sutton, S. G. J. Mochrie, and T. Greytak. Observation of speckle by diffraction with coherent X-rays. *Nature*, 352:608–610, 1991.

[12] C. Gutt, T. Ghaderi, M. Tolan, S. K. Sinha, and G. Grübel. Effects of partial coherence on correlation functions measured by x-ray photon correlation spectroscopy. *Phys. Rev. B*, 77:094133, 2008.

[13] S. K. Sinha, M. Tolan, and A. Gibaud. Effects of partial coherence on the scattering of x rays by matter. *Phys. Rev. B*, 57:2740–2758, 1998.

[14] D. M. Mills. *Third-generation hard x-ray synchrotron radiation sources : source properties, optics, and experimental techniques*. Wiley, New York, 2002.

[15] M. Tolan and S. K. Sinha. X-ray scattering with partial coherent radiation: The exact relationship between resolution and coherence. *Physica B: Condensed Matter*, 248(14):399 – 404, 1998.

[16] O. K. C. Tsui, S. G. J. Mochrie, and L. E. Berman. Statistical Analysis of X-ray Speckle at the NSLS. *Journal of Synchrotron Radiation*, 5(1):30–36, Jan 1998.

[17] O. G. Shpyrko, E. D. Isaacs, J. M. Logan, Y. J. Feng, G. Aeppli, R. Jaramillo, H. C. Kim, T. F. Rosenbaum, P. Zschack, M. Sprung, S. Narayanan, and A. R. Sandy. Direct measurement of antiferromagnetic domain fluctuations. *Nature*, 447(7140):68–71, 2007.

[18] S. Konings, C. Schussler-Langeheine, H. Ott, E. Weschke, E. Schierle, H. Zabel, and J. B. Goedkoop. Magnetic Domain Fluctuations in an Antiferromagnetic Film Observed with Coherent Resonant Soft X-Ray Scattering. *Physical Review Letters*, 106(7):077402, 2011.

[19] S. W. Chen, H. Guo, K. A. Seu, K. Dumesnil, S. Roy, and S. K. Sinha. Jamming behavior of domains in a spiral antiferromagnetic system. *Phys. Rev. Lett.*, 110:217201, 2013.

[20] G. Gr˙ Correlation spectroscopy with coherent x-rays. *Journal of Alloys and Compounds*, 362(12):3–11, 2004.

[21] B. J. Berne and R. Pecora. *Dynamic Light Scattering: With Applications to Chemistry, Biology, and Physics*. Dover Books on Physics Series. Dover Publications, 2000.

[22] J. C. Earnshaw. Surface light scattering: a methodological review. *Appl. Opt.*, 36(30):7583–7592, 1997.

[23] W. Brown. *Dynamic light scattering: the method and some applications*. Monographs on the physics and chemistry of materials. Clarendon Press, 1993.

[24] C. Gutt, T. Ghaderi, V. Chamard, A. Madsen, T. Seydel, M. Tolan, M. Sprung, G. Grübel, and S. K. Sinha. Observation of heterodyne mixing in surface x-ray photon correlation spectroscopy experiments. *Phys. Rev. Lett.*, 91:076104, 2003.

[25] A. Madsen, T. Seydel, M. Sprung, C. Gutt, M. Tolan, and G. Grübel. Capillary waves at the transition from propagating to overdamped behavior. *Phys. Rev. Lett.*, 92:096104, 2004.

[26] H. Z. Cummins. *Photon correlation spectroscopy and velocimetry*, volume 23. Plenum Pub Corp, 1977.

[27] D. Lumma and L. B. Lurio. Area detector based photon correlation in the regime of short data batches: Data reduction for dynamic x-ray scattering. *Review of Scientific Instruments*, 71(9):3274–3289, 2000.

[28] S. B. Dierker, R. Pindak, R. M. Fleming, I. K. Robinson, and L. Berman. X-ray photon correlation spectroscopy study of brownian motion of gold colloids in glycerol. *Phys. Rev. Lett.*, 75:449–452, 1995.

[29] T. Thurn-Albrecht, W. Steffen, A. Patkowski, G. Meier, E. W. Fischer, G. Grübel, and D. L. Abernathy. Photon correlation spectroscopy of colloidal palladium using a coherent x-ray beam. *Phys. Rev. Lett.*, 77:5437–5440, 1996.

[30] S. Brauer, G. B. Stephenson, M. Sutton, R. Brüning, E. Dufresne, S. G. J. Mochrie, G. Grübel, J. Als-Nielsen, and D. L. Abernathy. X-ray intensity fluctuation spectroscopy observations of critical dynamics in fe_3al. *Phys. Rev. Lett.*, 74:2010–2013, 1995.

[31] H. Kim, A. Rühm, L. B. Lurio, J. K. Basu, J. Lal, D. Lumma, S. G. J. Mochrie, and S. K. Sinha. Surface dynamics of polymer films. *Phys. Rev. Lett.*, 90:068302, 2003.

[32] Z. Jiang, H. Kim, X. Jiao, H. Lee, Y.-J. Lee, Y. Byun, S. Song, D. Eom, C. Li, M. H. Rafailovich, L. B. Lurio, and S. K. Sinha. Evidence for viscoelastic effects in surface capillary waves of molten polymer films. *Phys. Rev. Lett.*, 98:227801, 2007.

[33] W. S. Boyle and G. E. Smith. Charge coupled semiconductor devices. *Bell System Technical Journal*, 49(4):587–593, 1970.

[34] E. Jakeman. Speckle statistics with a small number of scatterers. *Optical Engineering*, 23(4):234453, 1984.

[35] E. Bartsch, V. Frenz, S. Kirsch, W. Schrtl, and H. Sillescu. Multi-speckle autocorrelation spectroscopy a new strategy to monitor ultraslow dynamics in dense and nonergodic media. In T. Palberg and M. Ballauff, editors, *Optical Methods and Physics of Colloidal Dispersions*, volume 104 of *Progress in Colloid and Polymer Science*, pages 40–48. Steinkopff, 1997.

[36] P. N. Pusey and W. Van Megen. Dynamic light scattering by non-ergodic media. *Physica A: Statistical Mechanics and its Applications*, 157(2):705 – 741, 1989.

[37] G. L. Squires. *Introduction to the Theory of Thermal Neutron Scattering*. Dover books on physics. Dover Publications, 1978.

[38] See nist website: http://www.ncnr.nist.gov/resources/sldcalc.html.

[39] V. F. Sears. Neutron scattering lengths and cross sections. *Neutron News*, 3(3):26–37, 1992.

[40] J. Lekner. *Theory of Reflection: Of Electromagnetic and Particle Waves*. Developments in Electromagnetic Theory and Applications. Springer, 1987.

[41] S. K. Sinha, E. B. Sirota, S. Garoff, and H. B. Stanley. X-ray and neutron scattering from rough surfaces. *Phys. Rev. B*, 38:2297–2311, 1988.

[42] L. G. Parratt. Surface studies of solids by total reflection of x-rays. *Phys. Rev.*, 95:359–369, Jul 1954.

[43] J. Daillant and A. Gibaud. *X-ray and Neutron Reflectivity: Principles and Applications*. Lecture Notes in Physics. Springer, 2009.

[44] J. Penfold and R. K. Thomas. The application of the specular reflection of neutrons to the study of surfaces and interfaces. *Journal of Physics: Condensed Matter*, 2(6):1369, 1990.

[45] T. P. Russell. X-ray and neutron reflectivity for the investigation of polymers. *Materials Science Reports*, 5(4):171–271, 1990.

[46] H. Zabel. X-ray and neutron reflectivity analysis of thin films and superlattices. *Applied Physics A*, 58(3):159–168, 1994.

[47] M.R. Fitzsimmons, S.D. Bader, J.A. Borchers, G.P. Felcher, J.K. Furdyna, A. Hoffmann, J.B. Kortright, Ivan K. Schuller, T.C. Schulthess, S.K. Sinha, M.F. Toney, D. Weller, and S. Wolf. Neutron scattering studies of nanomagnetism and artificially structured materials. *Journal of Magnetism and Magnetic Materials*, 271(1):103–146, 2004.

[48] E. Merzbacher. *Quantum Mechanics*. Wiley, 1998.

[49] G. P. Felcher, R. O. Hilleke, R. K. Crawford, J. Haumann, R. Kleb, and G. Ostrowski. Polarized neutron reflectometer: A new instrument to measure magnetic depth profiles. *Review of Scientific Instruments*, 58(4):609, 1987.

[50] C. F. Majkrzak. Polarized neutron reflectometry. *Physica B: Condensed Matter*, 173(12):75–88, 1991.

[51] C. F. Majkrzak. Neutron scattering studies of magnetic thin films and multilayers. *Physica B: Condensed Matter*, 221(14):342–356, 1996.

[52] T. Chatterji. *Neutron Scattering from Magnetic Materials*. Elsevier Science, 2005.

3 Magnetic Domain Dynamics in a Spiral Antiferromagnetic System

3.1 Abstract

Using resonant magnetic x-ray photon correlation spectroscopy, we show that the domains of a spiral antiferromagnet enter a jammed state at the onset of long-range order. We find that the the slow thermal fluctuations of the domain walls exhibit a compressed exponential relaxation with an exponent of 1.5 found in a wide variety of solid-like jammed systems and can be qualitatively explained in terms of stress release in a stressed network. As the temperature decreases, the energy barrier for fluctuations becomes large enough to arrest further domain wall fluctuations, and the domains freeze into a spatial configuration within 10 K of the Néel temperature. The relaxation times can be fitted with the Vogel-Fulcher law as observed in polymers, glasses and colloids thereby indicating that the dynamics of domain walls in an ordered antiferromagnet exhibit some of the universal features associated with jamming behavior.

3.2 Introduction

One of the most satisfying aspects of condensed matter physics is that a variety of condensed matter systems show universal behavior, i.e. behavior that

appears to be common to a wide variety of unrelated systems. A jamming transition occurs when the density of particles becomes large enough and the motion of the particles is restricted by the surrounding particles. In this regime, the particles cannot fluctuate freely but move collectively via long range interactions. Recently, there has been much interest in jamming transitions [1, 2], which were originally studied as a way to discuss the behavior of granular materials [3] or dense assemblies of particles, but have been eventually proposed as a more general and unified way of looking at dynamics of systems as diverse as structural glasses [4], entangled polymers [5, 6], colloidal gels [7], supercooled liquids [8], and the like. Jamming occurs when the particle densities or entanglements are such that the motions of the individual particles become very restricted so that they slow down. The fluctuations which occur in a jammed system e.g. a colloidal gel, with long-range interactions are cooperative fluctuations where a local displacement causes an inhomogeneity which is correlated with a displacement in another region. A theory based on elastic strains as the source of long-range interactions has been shown [9, 10] to yield an intermediate scattering function $F(Q,t)$ which decays as a compressed exponential $exp(-t/\tau)^{\beta}$, where the exponent β is $\sim 3/2$. This has been seen in colloidal gels via dynamical light scattering and X-ray Photon Correlation Spectroscopy (XPCS), as well as in other soft matter systems [10, 11]. Interestingly, similar behavior was observed in antiferromagnetic Cr metal using XPCS [12]. Up to now, domain wall dynamics under a magnetic field have been extensively studied in ferromagnets [13, 14]. However, purely thermally driven domain wall fluctuations in antiferromagnetic systems have been scarcely investigated, while these might be of importance for the discussions of noise issues in magnetic nanodevices. Unlike domains in a ferromagnetic material, the energetics of domain rearrangements in an antiferromagnet are not affected by macroscopic magnetic field energies, but are complicated by the breaking of translational symmetry.

We show in this chapter that the domain walls of the spiral antiferromagnet dysprosium undergo slow fluctuations near the Néel temperature which show essentially the same quantitative relaxational behavior as in Cr. As we discuss below,

the magnetic domains that form when an antiferromagnet orders are essentially in a jammed state, similar to particles with a repulsive interaction in a jammed granular system. We also observe that the domain dynamics freeze about 10K below the Néel temperature and the behavior shows remarkable similarity to glassy behavior observed in other systems. A very similar system, namely the spiral antiferromagnet Holmium was recently investigated using XPCS [15] and similar slow fluctuations were observed. However, the Ho film was only 11 monolayers thick and no quantitative analysis was carried out on the measured $F(Q,t)$.

3.3 Experiments

3.3.1 Sample

In this study we used an epitaxially grown Yttrium(Y)/ Dysprosium(Dy)/ Yttrium(Y) sample with the 500nm-thick Dy being the active layer [16]. Y/Dy/Y epitaxial trilayers were grown by molecular beam epitaxy. A (110) Nb buffer was grown at 800 °C on the $(11\bar{2}0)$ Al_2O_3 substrate in order to avoid rare earth oxidation from the substrate during deposition. Y(50 nm) and Dy(500 nm) layers were evaporated from an electron gun and an effusion cell, respectively. The growth direction for Y and Dy on (110) Nb is along [0001]. Structural and magnetic characterizations were performed by large angle x-ray scattering and SQUID magnetometry.

Dy has a hexagonal close packed structure, is paramagnetic above 180 K (T_N) and exhibits an incommensurate helical spin structure in the temperature range 89 K $-$ 180 K along the c$-$axis with ferromagnetic alignment of the moments in basal plane [17] (Figure 3.1). The helical magnetic phase is due to indirect exchange interactions between the Dy moments and in real space these can be represented by exchange interactions which oscillate in sign versus distance: positive for nearest neighbors, but negative for next nearest neighbors. At 89 K, bulk Dy undergoes a first order antiferromagnetic(AFM) $-$ ferromagnetic(FM) phase transition when the magnetostrictive energy overtakes the exchange energy. In a thin film, however, this can be reduced or enhanced depending on the film thickness,

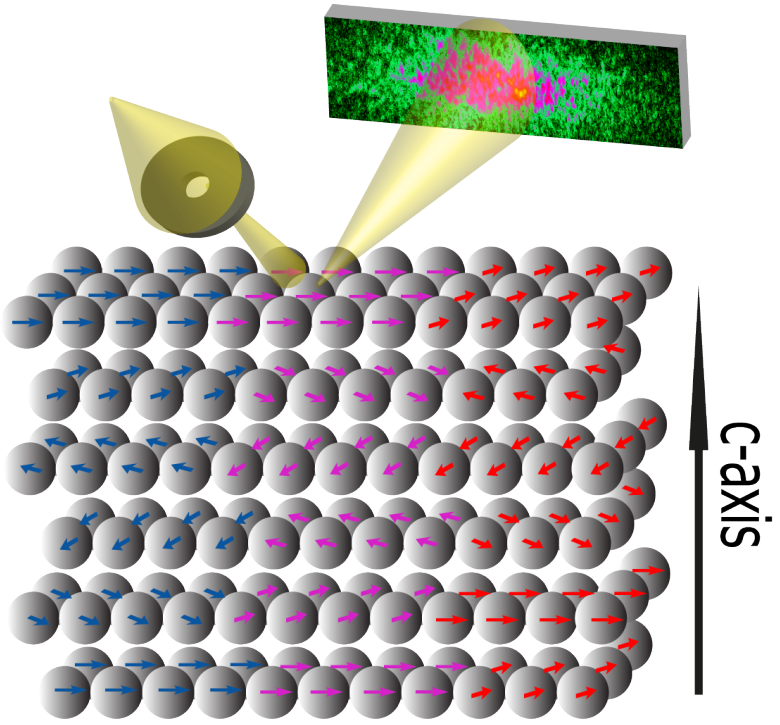

Figure 3.1: Schematic of the coherent x-ray experiment set-up. Dysprosium exhibits a spiral antiferromagnetic structure between its T_C and T_N. The long period along the c-axis gives superlattice diffraction peak around charge reflection peak.

strains etc [18, 19].

3.3.2 Experiments at the Advanced Light Source

Coherent x-ray scattering experiments were carried out at beamline 12.0.2.2 of the Advanced Light Source, Lawrence Berkeley National Laboratory (Figure 3.2). A linearly polarized incident x-ray beam was tuned to the Dy M_5 edge at 1297 eV to access the charge-forbidden (0, 0, Q_m) AF Bragg peak via resonant magnetic scattering in reflection geometry. A 5μm diameter pinhole was put in the beam path (1 mm upstream) to establish transverse coherence of the incident x-ray beam. The pinhole and the sample were mounted on the same stage to avoid any relative motion. Speckle patterns were recorded with an Andor charge coupled device (CCD) camera (DO-436) consisting of 2048 by 2048 pixels with pixel size

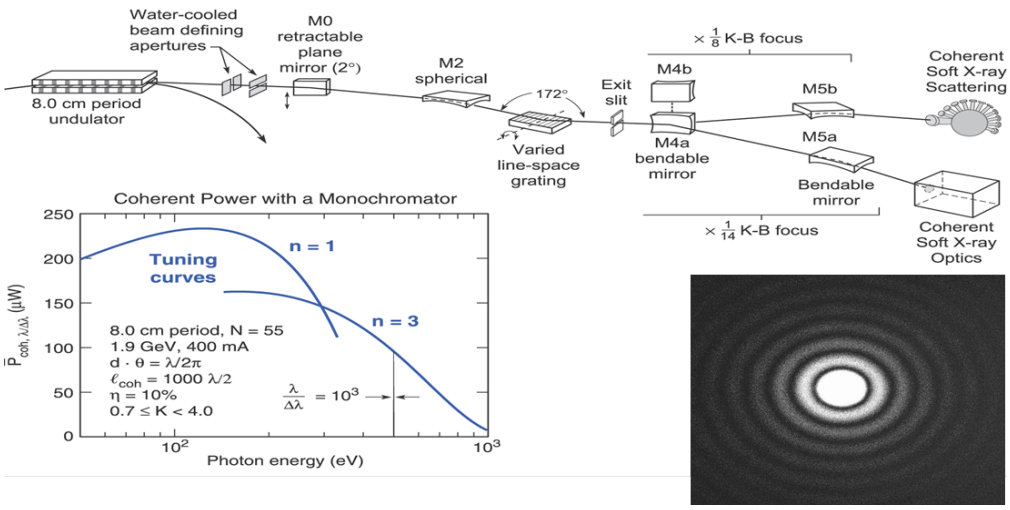

Figure 3.2: Beamline 12.0.2.2 at the Advanced Light Source, Lawrence Berkeley National Laboratory. The coherent flux at 500eV is $\sim 5 \times 10^9$ phtons/sec/0.1%BW. Then Airy pattern due to difraction from 2.5 μm pinhole at $\lambda = 2.48$ nm is also shown here. Figure courtesy of the ALS beamline.

of 13.5μm by 13.5 μm, 0.45 m downstream the sample. The optical contrast of the speckles, which is defined as $(I_{max} - I_{min})/(I_{max} + I_{min})$ is $\sim$ 0.15 - 0.22, depending on the scattering angle and thus varies with temperature. The CCD was cooled to -50 °C to reduce noise level. A 10-frame-averaged dark image was taken with the beam off and was subtracted from every data frame. The intensity of each pixel was normalized by the incident beam intensity. The intensity-intensity autocorrelation function was then calculated for each pixel within the whole diffraction peak area and then averaged. The analog/digital unit (ADU), which is the detector counts corresponding to a single photon, is $\sim$ 133 at x-ray energy of 1297eV, and the pixels with counts smaller than 30 were not taken into account in the calculation. For each measurement we have raised the temperature above T_N, then reduced it to the measurement temperature and waited for one hour until the temperature was stabilized within 10 mK. A two-hour long movie of the evolving speckle pattern was subsequently taken with frame time resolution of 5 sec.

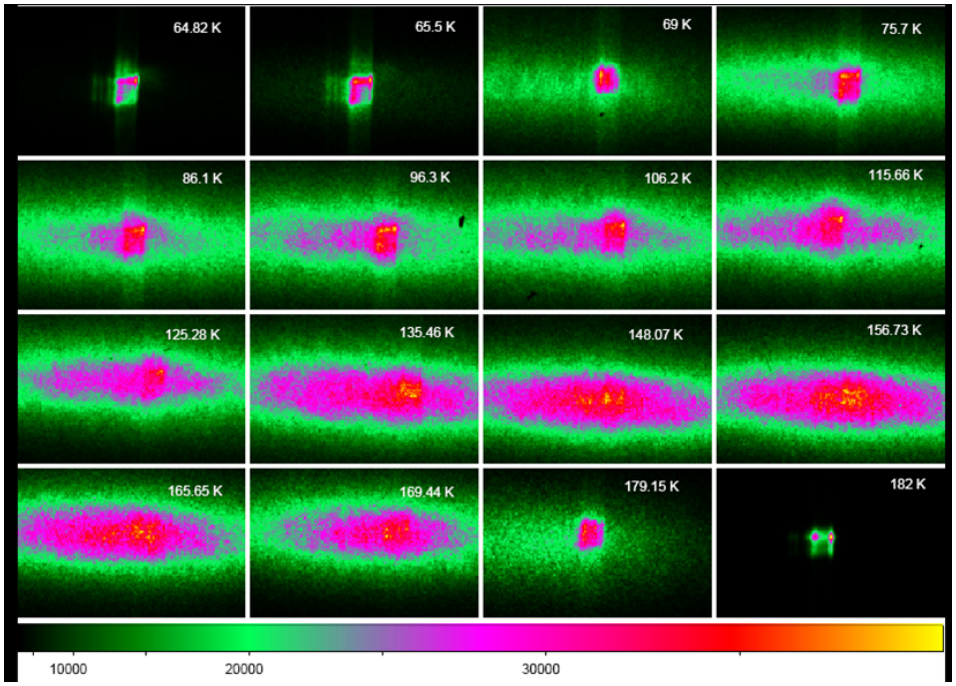

Figure 3.3: Evolution of the (0, 0, Q_m) diffraction peak as a function of temperature. The measurement was done with incoherent resonant x-ray. It shows that the T_C is $\sim$ 63K upon cooling and T_N is 180K. Below T_C and above T_N, reflection peak remains.

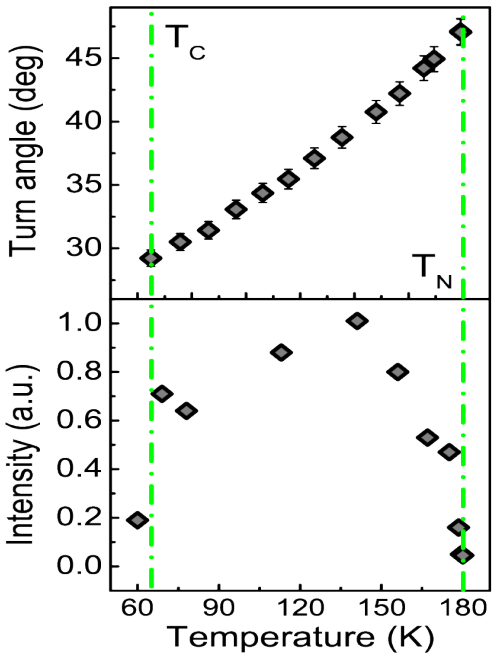

Figure 3.4: (Top) Spins turning angle between layers of basal planes as a function of temperature. The turning angles were determined by the diffraction peak position. (Bottom) Integrated intensity on the CCD as a function of temperature.

3.4 Results and Discussions

The helical spin structure gives rise to magnetic satellite peaks along the specular direction at Q = (0, 0, l$\pm$Q$_m$), in units of reduced reciprocal lattice vectors, where l is an even integer. Figure 3.3 shows the evolution of the (0, 0, Q$_m$) AFM Bragg peak as a function of temperature which shows T$_N$ = 180 K and T$_C$ = 63 K. Note that the phase transition is first order at T$_C$ (AFM - FM transition) and second order at T$_N$ (AFM - paramagnetic transition). The position of the magnetic satellite at Q$_m$ varies with temperature because the turn angle between spins in adjacent basal planes changes (Figure 3.4). To determine the lateral correlation length ξ, we fit the envelope of the Bragg peak along Q$_y$ with a Lorentzian to the 3/2 power as theoretically expected for random 2D domains [20, 21, 22]

$$I(Q_y) \propto \frac{\xi^2}{(1+Q_y^2\xi^2)^{3/2}} \tag{3.1}$$

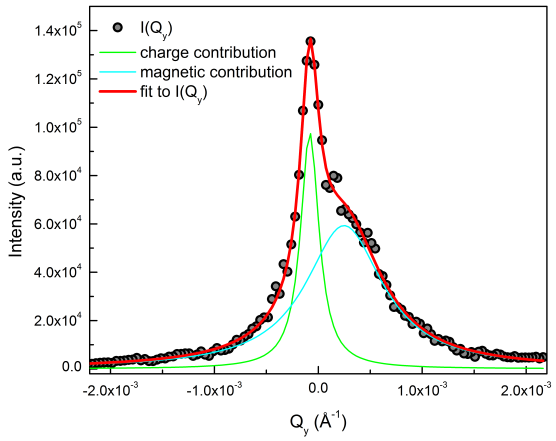

Figure 3.5: An example of the fitting to the lateral correlation length at T = 176.63 K. The center of the charge peak (which is centered about the normal of the physical surface) and that of the magnetic peak are not coincident because there is a slight difference in surface normal direction and the c-axis of the dysprosium crystal.

The magnetic domain size is $\sim 6\xi$. The temperature independent charge scattering due to the surface roughness was fitted with a separate Lorentzian that yielded a correlation length of 400 nm (Figure 3.5). No significant change in the correlation length or the dynamics were observed as a function of time over a period of two hours at each temperature, indicating that aging effects were too slow to observe and that the domains were in at least metastable equilibrium during the measurements. We found that the magnetic lateral correlation length increases rapidly below the ordering temperature but saturates at a value of 100 nm for T $<$ 177 K (Figure 3.6). We note that neutron [23] and X-ray [24] imaging of similar spiral magnetic domains in Ho yield domain sizes of the order of microns. However, these imaging measurements were sensitive only to the change of chirality but not other defects, such as spin-slip [25], which probably limit the lateral spiral spin correlations to the smaller values observed in our study, and in other studies of Dy magnetic domains based on scattering techniques [26]. The correlation length along the c-axis (perpendicular to the film surface) can also be determined by

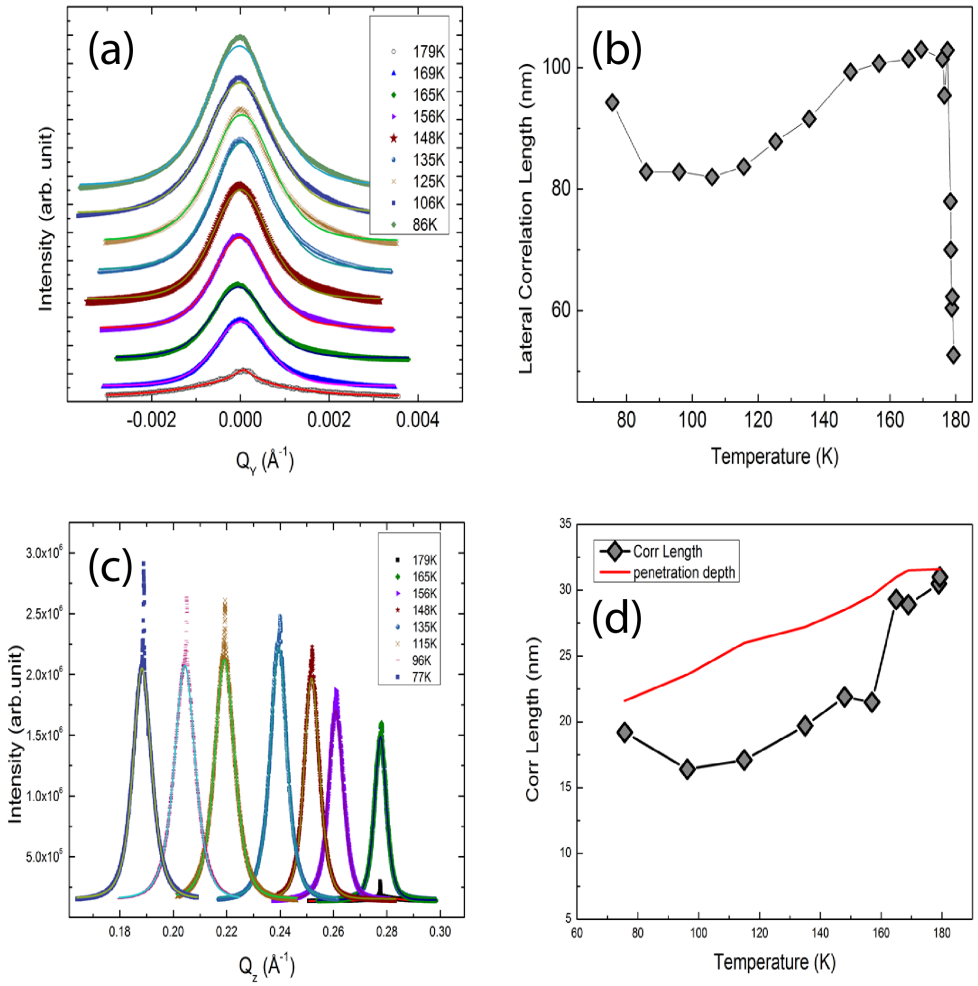

Figure 3.6: (a) Integrated intensity along Q_y at all temperature range and the Lorentzian 3/2 power fits to them. At the low temperature range ($63K < T < 179K$), the charge scattering is relatively small compared to the magnetic scattering. (b) The lateral correlation length as a function of temperature. (c) Integrated intensity along Q_x - Q_z axis and the fits to them. (d) The vertical correlation length extracted from the Lorentzian fits. The red line indicates the penetration depth. It is a function of temperature because the incident angles (in order to reach diffraction peak) changed.

fitting the peak in Q_x-Q_z direction, and it is limited by the penetration depth of soft X-rays into Dy ($\sim$ 20 nm, see Figure 3.6). Thus we are only sensitive to the domains close to the top Y/Dy interface.

X-ray Photon Correlation Spectroscopy (XPCS) is a technique for using a coherent X-ray beam to obtain the real time intermediate scattering function F(Q,t) i.e. the Fourier transform of S(Q,ω) for long times, analogous to what is done in Dynamical Light Scattering. The coherence of the X-ray beam results in the interference pattern of the scattered x-rays manifesting itself as speckle, which represents a fingerprint of the scattering system. The scattered intensity around the (0, 0, Q_m) satellite position essentially disappears below T_C and above T_N which means that the speckle we observe in the AF spiral phase is primarily magnetic in origin and arises due to fluctuations of the spin arrangements out of the perfect spiral order [15, 27] with some additional weak scattering from the surface roughness. By taking N successive images with shutter time of $\Delta\ t$ for a time span of S, where $S \gg \Delta\ t$, a movie of the speckle pattern can be created. Analyzing the time series allows us to calculate the autocorrelation function and determine the temporal evolution of the fluctuating domain walls for varying time delays $(t_n - t_0)$, $n = 0, 1, 2, ..., N$ over a time span S.

In Figure 3.7(a) we show snapshots of the speckle pattern every 250 seconds at a fixed temperature of 178.50 K. Inspection shows that the speckle pattern is changing with time which is indicative of fluctuating domain walls. In contrast to driven dynamics, as would be the case if the domains were driven with an external stimulus [13, 14], such as a magnetic field, the dynamics that we observe are self-sustained and thermally activated. To quantify the dynamic behavior we calculate the intensity-intensity autocorrelation function g_2 from the time series speckle data which is defined as [28]:

$$g_2(Q,t) = \frac{\langle I(Q,t')I(Q,t'+t)\rangle_{t'}}{\langle I(Q,t')\rangle_{t'}^2} = 1 + A|F(Q,t)|^2 \tag{3.2}$$

where $I(Q,t')$ is the intensity at wavevector Q at a time t', t is the time delay, and angular brackets represent averages over the subscripted variable. $F(Q,t)$ is the intermediate scattering function and A is the speckle contrast.

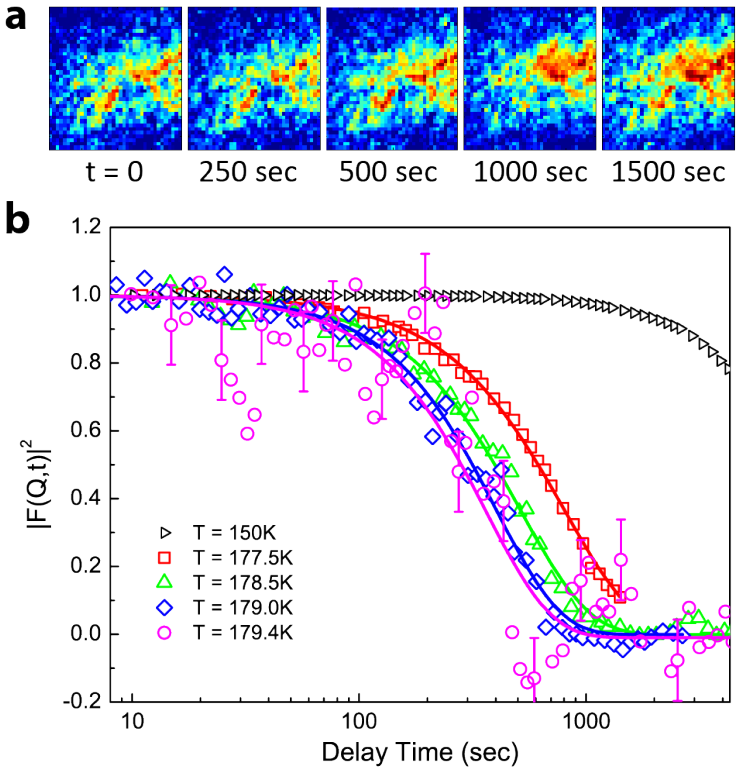

Figure 3.7: (a) Time snapshot of the speckles at 178.50 K taken every 250 sec. Changing speckle pattern with time indicates dynamics. (b) Normalized autocorrelation function as a function of temperature. The correlation is calculated from the time series of the (0,0,Q_m) Bragg peak intensity. All speckles in the Bragg peak are taken into account. The increasingly faster dynamics towards T_N is evident. A compressed exponential function was used to fit the data. Solid lines are fit to the data. Error bars are not shown when they are comparable to or smaller than the size of the points.

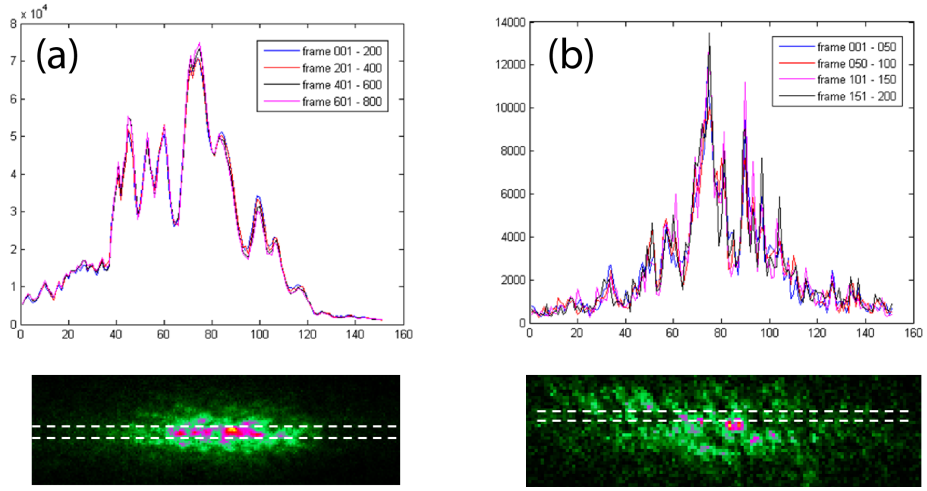

Figure 3.8: Line-cuts through the diffraction peak as shown in the bottom panel for (a) T = 150.0 K and (b) 178.5 K. The line-cuts were time-averaged over 1000 seconds for (a) and 250 seconds for (b). The line-cut in (a) shows a static case over $\sim$ 4000 seconds, and the line-cut in (b) shows dynamics in the speckle patterns over this time scale.

The $|F(Q,t)|^2$ (Figure 3.7(b)) shows strong temperature dependence. We observe dynamics only near T_N. The dynamics are fastest near T_N and gradually get arrested within 10 K below T_N. For T <175 K (e.g. at 150 K as shown in Figure 3.7(b)) the autocorrelation curve is almost constant within the same time span of measurement and the time constant is beyond the instrumental stability. Another way to look at the speckle dynamics is to look at the speckle visibility, as shown in Figure 3.8. Figure 3.8 shows line-cuts through the magnetic diffraction peak at (a) 150.0 K and (b) 178.5 K. The line-cuts show a random speckle pattern on top of the diffraction peak. The line cuts were also time-averaged over 1000 seconds for 150.0 K and 250 seconds for 178.5 K to obtain better statistics. At 150.0 K, the line-cut was basically unchanged over a time scale of 4000 seconds. At 178.5 K, however, the line-cut showed dramatic difference between every 250 second, which indicates the speckles fluctuated on this time scale. The dynamics that we observe are not due to critical spin fluctuations which occur at a few tens of nm length scales at GHz frequency or greater [29]. We observe a smooth decaying curve which is not a simple exponential but a compressed exponential,

indicative of the presence of a distribution of decay times due to fluctuating walls in a disordered domain wall network.

In the present case the intermediate scattering function F(t) has been fitted with the expression

$$|F(t)| = exp(-(t/\tau)^{\beta}) \tag{3.3}$$

where τ is the decay constant and β is the stretching exponent. We found $\beta \simeq 1.5$ for all the curves at all measured temperatures (Fig. 3(a), inset). A value of $\beta > 1$ signifies collective motion which means that the domain walls in Y/Dy/Y exhibit cooperative behavior most likely due to the long range nature of the RKKY interaction ($J_{RKKY} \propto 1/r^3$) which plays a significant role in establishing the spiral structure in this material. More importantly, an exponent of ~ 1.5 has been found in the jammed state of a wide variety of systems including colloidal gels [10], concentrated emulsions, dense ferro-fluids [30] and Cr [12]. In these disordered systems freezing of the fluctuations takes place and the dynamic behavior corresponds to non-diffusive motion that can be semi-quantitatively explained in terms of the relaxation of long-range elastic strains in a stressed network [10]. We note that this explanation may also apply to Cr since the Cr spins interact via a long range exchange interaction as well, dominated by Fermi surface effects and the conduction band structure. This will yield the $\beta \sim 1.5$ observed in the temperature range just below T_N. Domain dynamics in Cr are however drastically different at low temperature where they are driven by quantum tunneling down to 4K. Such a phenomenon is not observed in the case of Dy, most likely because of the localized nature of the magnetic moments in this material.

The physical processes underlying this behavior are as follows: As one approaches the Néel temperature from above ($T_N = 180$ K), the spin-spin correlation length diverges, but the antiferromagnetic fluctuating clusters which form may have different spin orientations in the basal plane, or opposite chiralities. Below T_N, these clusters become domains and are head to head with each other leading to frustration, thus the domains are in a jammed state as soon as the long-range order sets in. In this regime there are normal spin wave excitations, and there are also slow thermal fluctuations of the spins in the domain walls which form

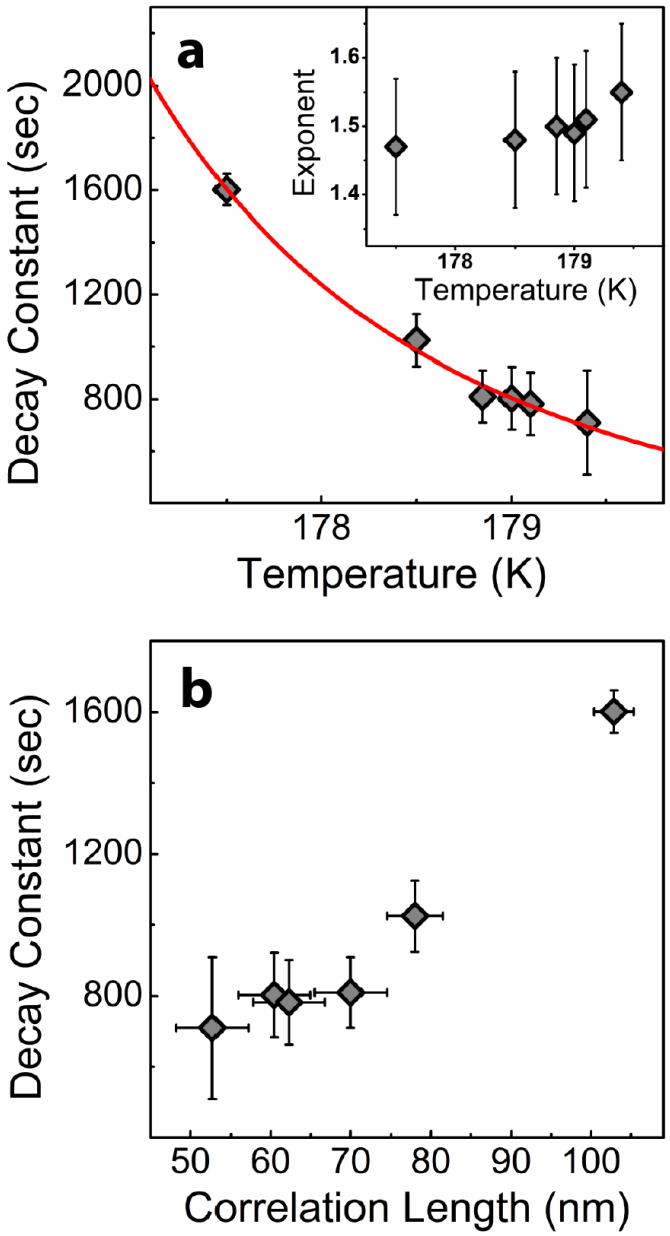

Figure 3.9: (a) Decay constants obtained from the fitting of the autocorrelation curves in Figure 3.7. The red line is a Vogel-Fulcher function fit to the data. Within experimental accuracy we found $\beta = 1.5$ for all the temperatures (inset). (b) The decay constant versus correlation length. The dynamics slow down as the correlation length increases.

a disordered network. These thermally excited spin fluctuations set up a stress field in the domain wall network which are released by other spin fluctuations at a later time t. The fluctuations thus involve correlated fluctuations of the spins and results in the domain wall fluctuations due to the long-range nature of the RKKY interaction, and results in the compressed exponent 1.5. In most of the jammed systems, there is also a Q^{-1} dependence of the time constant [10], but we were not able to study the Q-dependence because of the limited range due to the diffraction geometry. We observe the dynamics only when the temperature is very close to T_N. As the temperature is lowered, the energy required to flip spins and the anisotropy energy increase which results in reducing domain wall fluctuations. At $\sim$ 177 K the time constant for the fluctuations becomes extremely large, reminiscent of a glassy state.

In analogy to glasses or jammed systems, for gradually freezing domain dynamics we expect that the decay constant should show super Arrhenius behavior [31]. In Fig. 3(a) we plot the decay constant as a function of temperature and fit the data with the Vogel–Fulcher (VF) function of the form

$$\tau^{-1} = \tau_0^{-1} exp(-DT_0/(T - T_0)) \tag{3.4}$$

We obtain a good fit with T_0 = 171 K and the fragility parameter D = 0.14. We note that for pure Arrhenius behavior the fragility parameter should approach infinity. However, another way of looking at Eq. (4) is simply that we have a strongly temperature dependent activation energy. Fig 3(b) shows the decay constant as a function of correlation length. The dynamics do get slower as the correlated regions grow in size, which suggests that the freezing behavior depends on the size of the domains [32]. A close relation between the energy barriers for domain wall fluctuations and for domain growth is indeed expected.

3.5 Conclusion

To summarize, we provide evidence of the jamming behavior of domains in a single crystal spiral antiferromagnet. We observe that the domains enter a jammed state as soon as the long range order sets-in. The dynamics show a

collective behavior as evidence by compressed exponent 1.5, and exhibit a super Arrhenius behavior that can be well described by a Vogel-Fulcher function with a divergence of relaxation time. We also show that the decay constant τ is tied to the domain size. For temperature just below T_N, the domains fluctuate, but increasingly get frozen as the temperature shifts towards T_0. We speculate that this behavior is the origin of the blocking temperature that is often observed in antiferromagnets [33]. The theoretical treatment of jamming transitions, together with computer simulations and experiments on model systems, is quite robust [7, 32, 1, 34, 35] and explains many aspects of kinetic freezing type phase transitions. The concept of a jamming transition has not hitherto been applied to magnetic systems but appears to manifest itself in the slow collective dynamics of domain walls below the ordering temperature. Our study shows that domain dynamics near the Néel temperature show many aspects similar to those in supercooled liquids, polymers, colloidal gels, glasses etc. and bolsters the evidence for the universal nature of the jamming transition in discussing the freezing behavior of disordered and frustrated systems. Due to the restriction in time scales for the experiments, the data is somewhat limited in the range of time scales which could be probed for this system. Future experiments are planned on other systems which will enable us to look for universal behavior associated with domain growth in antiferromagnetic systems when they order via a continuous transition from a paramagnetic state.

The work at LBNL including experiment at ALS was supported by the Director, Office of Science, Office of Basic Energy Sciences, of the U.S. Department of Energy under Contract No. DEAC02-05CH11231. Work at UCSD was supported by Basic Energy Sciences, U.S. Dept. of Energy under Grant Number: DE-SC0003678. The text in this chapter is based on the material published in S. -W. Chen, H. Huo, K. A. Seu, K. Dumesnil, S. Roy and S. K. Sinha. Jamming behavior of domains in a spiral antiferromagnetic system. *Phys. Rev. Lett.*, 110, 217201 (2013).

Bibliography

[1] A. J. Liu and S. R. Nagel. Nonlinear dynamics - Jamming is not just cool any more. *Nature*, 396(6706):21–22, 1998.

[2] M. E. Cates, J. P. Wittmer, J. P. Bouchaud, and P. Claudin. Jamming, Force Chains, and Fragile Matter. *Physical Review Letters*, 81(9):1841–1844, August 1998.

[3] O. Dauchot, G. Marty, and G. Biroli. Dynamical heterogeneity close to the jamming transition in a sheared granular material. *Physical Review Letters*, 95(26):265701, 2005.

[4] T. R. Kirkpatrick, D. Thirumalai, and P. G. Wolynes. Scaling Concepts for the Dynamics of Viscous-Liquids near an Ideal Glassy State. *Physical Review A*, 40(2):1045–1054, 1989.

[5] P. Falus, S. Narayanan, A. R. Sandy, and S. G. J. Mochrie. Crossover from stretched to compressed exponential relaxations in a polymer-based sponge phase. *Physical Review Letters*, 97(6):066102, 2006.

[6] H. Y. Guo, G. Bourret, M. K. Corbierre, S. Rucareanu, R. B. Lennox, K. Laaziri, L. Piche, M. Sutton, J. L. Harden, and R. L. Leheny. Nanoparticle Motion within Glassy Polymer Melts. *Physical Review Letters*, 102(7):075702, 2009.

[7] V. Trappe, V. Prasad, L. Cipelletti, P. N. Segre, and D. A. Weitz. Jamming phase diagram for attractive particles. *Nature*, 411(6839):772–5, June 2001.

[8] P. G. Debenedetti and F. H. Stillinger. Supercooled liquids and the glass transition. *Nature*, 410(6825):259–67, March 2001.

[9] J. P. Bouchaud and E. Pitard. Anomalous dynamical light scattering in soft glassy gels. *The European Physical Journal E*, 236:231–236, 2001.

[10] L. Cipelletti, L. Ramos, S. Manley, E. Pitard, D. A. Weitz, E. E. Pashkovski, and M. Johansson. Universal non-diffusive slow dynamics in aging soft matter. *Faraday Discussions*, 123:237–251, 2003.

[11] X. Lu, S. Mochrie, S. Narayanan, A. Sandy, and M. Sprung. How a Liquid Becomes a Glass Both on Cooling and on Heating. *Physical Review Letters*, 100(4):045701, January 2008.

[12] O. G. Shpyrko, E. D. Isaacs, J. M. Logan, Y. J. Feng, G. Aeppli, R. Jaramillo, H. C. Kim, T. F. Rosenbaum, P. Zschack, M. Sprung, S. Narayanan, and A. R. Sandy. Direct measurement of antiferromagnetic domain fluctuations. *Nature*, 447(7140):68–71, 2007.

[13] G. Durin and S. Zapperi. *The Science of Hysteresis: Physical Modeling, Micromagnetics and Magnetization Dynamics, vol. II, ch. III.* Cambridge University Press, Amsterdam, 2006.

[14] T. Mukherjee, M. Pleimling, and Ch. Binek. Probing equilibrium by nonequilibrium dynamics: Aging in Co/Cr superlattices. *Physical Review B*, 82(13):1–5, October 2010.

[15] S. Konings, C. Schussler-Langeheine, H. Ott, E. Weschke, E. Schierle, H. Zabel, and J. B. Goedkoop. Magnetic Domain Fluctuations in an Antiferromagnetic Film Observed with Coherent Resonant Soft X-Ray Scattering. *Physical Review Letters*, 106(7):077402, 2011.

[16] K. Dumesnil, C. Dufour, Ph. Mangin, G. Marchal, and M. Hennion. Magnetic structure of dysprosium in epitaxial Dy films and in Dy/Er superlattices. *Physical Review B*, 54(9):6407–6420, September 1996.

[17] R. J. Elliot. *Magnetic properties of Rare Earth Metals.* Plenum Publishing, London, 1972.

[18] R. W. Erwin, J. J. Rhyne, M. B. Salamon, J. Borchers, S. Sinha, R. Du, J. E. Cunningham, and C. P. Flynn. Magnetic-Structure of Dy-Y Superlattices. *Physical Review B*, 35(13):6808–6825, 1987.

[19] K. Dumesnil, C. Dufour, P. Mangin, G. Marchal, and M. Hennion. Magnetoelastic and Exchange Contributions to the Helical-Ferromagnetic Transition in Dysprosium Epitaxial-Films. *Europhysics Letters*, 31(1):43–48, 1995.

[20] P. Debye, Jr H. R. Anderson, and H. Brumberger. Scattering by an Inhomogeneous Solid. II. The Correlation Function and Its Application. *Journal of Applied Physics*, 28(6):679–683, 1957.

[21] S. W. Chen, H. Guo, K. A. Seu, K. Dumesnil, S. Roy, and S. K. Sinha. Jamming behavior of domains in a spiral antiferromagnetic system. *Phys. Rev. Lett.*, 110:217201, May 2013.

[22] See Appendix A.

[23] S. B. Palmer, J. Baruchel, A. Drillat, C. Patterson, and D. Fort. Influence of the purity on the domains and the elastic constants in the helimagnetic phases of Ho and Tb. *Journal of Magnetism and Magnetic Materials*, 54(0):1626–1628, 1986.

[24] J. C. Lang, D. R. Lee, D. Haskel, and G. Srajer. Imaging spiral magnetic domains in Ho metal using circularly polarized Bragg diffraction. *Journal of Applied Physics*, 95(11):6537–6539, 2004.

[25] D. Gibbs, D. E. Moncton, K. L. DAmico, J. Bohr, and B. H. Grier. Magnetic x-ray scattering studies of holmium using synchro- tron radiation. *Physical Review Letters*, 55(2):234–237, 1985.

[26] H. Ott, C. Schussler-Langeheine, E. Schierle, E. Weschke, and G. Kaindl. Depth-resolved magnetic structure across the ferromagnetic to helical-antiferromagnetic phase transition in Dy/W(110). *Physical Review B*, 82(21):214408, 2010.

[27] K. A. Seu, S. Roy, J. J. Turner, S. Park, C. M. Falco, and S. D. Kevan. Cone phase and magnetization fluctuations in Au/Co/Au thin films near the spin-reorientation transition. *Physical Review B*, 82(1):012404, 2010.

[28] M. Sutton. A review of X-ray intensity fluctuation spectroscopy. *Comptes Rendus Physique*, 9(5-6):657–667, 2008.

[29] B. D. Gaulin, M. Hagen, and H. R. Child. A Critical Scattering Study of the Helical Antiferromagnets Ho and Dy. *Journal De Physique*, 49(C-8):327–328, 1988.

[30] A. Robert, E. Wandersman, E. Dubois, V. Dupuis, and R. Perzynski. Glassy dynamics and aging in a dense ferrofluid. *Europhysics Letters*, 75(5):764–770, 2006.

[31] G. Tarjus, S. A. Kivelson, Z. Nussinov, and P. Viot. The frustration-based approach of supercooled liquids and the glass transition: a review and critical assessment. *Journal of Physics-Condensed Matter*, 17(50):R1143–R1182, 2005.

[32] A. S. Keys, A. R. Abate, S. C. Glotzer, and D. J. Durian. Measurement of growing dynamical length scales and prediction of the jamming transition in a granular material. *Nature Physics*, 3(4):260–264, 2007.

[33] H. C. Siegmann. Surface and 2D magnetism. *Journal of Physics: Condensed Matter*, 4(44):8395, 1992.

[34] C. S. O'Hern, L. E. Silbert, A. J. Liu, and S. R. Nagel. Jamming at zero temperature and zero applied stress: The epitome of disorder. *Physical Review E*, 68(1):011306, 2003.

[35] R. Bandyopadhyay, D. Liang, H. Yardimci, D. A. Sessoms, M. A. Borthwick, S. G. J. Mochrie, J. L. Harden, and R. L. Leheny. Evolution of particle-scale dynamics in an aging clay suspension. *Physical Review Letters*, 93(22):228302, 2004.

4 Non-switchable Magnetic Moments in polycrystalline and (111)-epitaxial Permalloy/CoO Exchange-biased Bilayers

4.1 Abstract

We have measured the interfacial magnetization depth profile in ferromagnet/antiferromagnet exchange-coupled NiFe/CoO bilayers. Both a polycrystalline and an epitaxial (111) bilayer were examined. We find that the non-switchable magnetization profile in the biased state is highly correlated with the magnetization profile in the unbiased state. The non-switchable moment distributions are shown to be consistent with the predictions of a previously reported model for the magnetic and microstructural features of the interfacial region.

4.2 Introduction

When a ferromagnet (FM) and an antiferromagnet (AFM) are exchange-coupled through an interface, and are field cooled through the ordering temperature of the AFM, or the FM is deposited below the AFM ordering temperature, the exchange bias effect (produced by the exchange anisotropy phenomenon) is observed [1]. The exchange bias effect is characterized by a shift of the hysteresis

loop of the FM along the cooling field axis by H_E, the exchange bias field, usually accompanied by an enhancement of the coercive field H_C. Currently, most magnetic storage systems with thin-film sensors utilize this effect. Since its discovery, there has been a significant research effort to understand the details of the mechanism and several well-documented reviews have been written in the past decade [2, 3, 4, 5, 6, 7, 8]. Yet a complete microscopic understanding of the details in any given AFM/FM bilayer system is still unclear.

Interfacial effects are crucial in the exchange bias system. Takano et al. [9] performed thermoremanent studies on the NiFe/CoO system and suggested a strong correlation between the uncompensated AFM spins and the unidirectional anisotropy. It is now generally accepted that the exchange bias effect depends strongly on these uncompensated spins (UCS) at the interface [10]. The shift of the hysteresis loops is produced by those UCS that are exchange coupled to the magnetic entities in the interfacial region as well as to the AFM. Some of these spins do not reverse completely when the applied field is reversed. We refer to them as non-switchable (NS) spins. The NS spins include the pinned spins in the AFM layer, as well as the spins coupled to them which form partial domain walls near the FM-AFM interface [11]. A more detailed discussion about the NS spins will be given in the discussion section. Because the interface is buried, measuring these NS spins is difficult. Penetrating probes, such as x-rays and neutrons, are thus some of the limited suitable tools for studying this [12, 13, 14, 15, 16, 17, 18, 19]. The problem is further complicated by the differences from system to system [8].

Permalloy (Py)/CoO bilayer is a widely studied exchange bias system because the ordering temperature of CoO ($T_N \sim 290$ K) is close to room temperature, the magnetic structure of CoO is well-known, and the soft magnetic properties of Py emphasize exchange-bias effects. There have been several reported studies of this system by various groups. Moran et al. [20] studied hysteresis loops of Py films deposited on CoO single crystals with [111] faces and found that increased disorder at the interface increased H_E. They noted that the domain structure of AFM CoO could present a combination of compensated and uncompensated AF spins at the interface. Moran and Schuller [21] studied the dependence of H_E on cooling

field and proposed a model where the perpendicular coupling between the AFM and FM spins might be responsible for the exchange bias. Gökemeijer et al. [10] carried out magnetization studies of Py deposited on CoO with [111], [110], [100] faces respectively and also polycrystalline CoO. They found zero values for H_E for the CoO [100] and [110] samples (which are nominally completely compensated), finite but small H_E values for the CoO [111] interface and larger values for the polycrystalline interface. The coercive field, however, was largest for the [100] sample and smallest for the polycrystalline sample. A recent combined magnetic x-ray scattering and polarized neutron diffraction study by Radu et al. [22] relates this behavior to the random orientations of the domains in the (111) textured system. However, in the previous studies, the nature of the interface magnetization was not studied. This can be studied with resonant magnetic x-ray reflectivity using circular polarization or with polarized neutron reflectivity.

Recent magnetic x-ray reflectivity studies reported that there is a thin interfacial layer in the polycrystalline Py/CoO system which has net Co moments above T_N [23, 24, 25]. The Co moments are pinned antiparallel to the cooling field in the biased state. In this Chapter, we have extended the previous studies and measured the polarized neutron reflectivity in both polycrystalline and (111)-epitaxial Py/CoO bilayers. The depth profiles of the non-switchable and switchable components of the magnetization in the vicinity of the Py/CoO interface are obtained and compared, and lead to new insights into the mechanism of exchange bias in this system.

4.3 Experiments

The polycrystalline Py/CoO bilayer was grown on a Si(100) substrate with the native oxide surface layer. Polycrystalline CoO ($\sim$ 15 nm) was deposited from a Co target by reactive sputtering in Ar and O_2. The Py ($\sim$ 20 nm) was deposited from a $Ni_{0.81}Fe_{0.19}$ target in an Ar atmosphere. The sample was capped with Ta ($\sim$ 4 nm) to prevent oxidation. The (111) epitaxial bilayer was grown on a Al_2O_3(0001) substrate and had the same thickness as the polycrystalline film. Both

Table 4.1: Thickness and roughness of the polycrystalline film and (111) epitaxial film, obtained by Cu K_α x-ray reflectivity measurement. The roughness corresponds to the surface above the layer. SLD is the scattering length density.

Polycrystalline film					(111)-epitaxial film				
Layer	Thickness ($\mathring{A}$)	Roughness ($\mathring{A}$)	SLD ($10^{-6}\mathring{A}^{-2}$)	Bulk SLD ($10^{-6}\mathring{A}^{-2}$)	Layer	Thickness ($\mathring{A}$)	Roughness ($\mathring{A}$)	SLD ($10^{-6}\mathring{A}^{-2}$)	Bulk SLD ($10^{-6}\mathring{A}^{-2}$)
Ta_2O_5	34.7	10.4	61.1	54.6	Ta_2O_5	30.0	8.4	56.9	54.6
Ta	30.6	5.5	108.7	104	Ta	29.7	8.5	108.6	104
Py	201.4	10.0	63.6	63.5	Py	206.9	9.8	63.1	63.5
CoO	163.0	6.7	46.5	47.2	CoO	161.8	6.2	47.1	47.2
Si	∞	5.6	20.0	20.1	Al_2O_3	∞	6.0	33.6	33.5

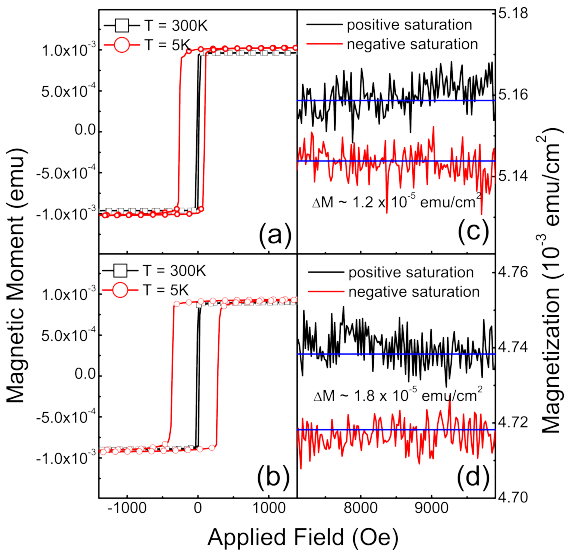

Figure 4.1: Hysteresis loop of (a) polycrystalline and (b) (111)-epitaxial Py/CoO film at 300 K and after cooling in 1.15 T field to 5 K. A negative exchange bias is observed in both samples. Magnetization at positive and negative saturation applied field (negative flipped for comparison) in (c) polycrystalline film and (d) epitaxial film show net positive non-switchable moments in both samples.

samples were characterized by x-ray reflectivity using a Cu K_α x-ray unit. The data was fit using a Parratt-type formalism [26] and the fitted structural/chemical profile is listed in Table I. The (111) epitaxial film was further characterized by x-ray diffraction and shows CoO(111) and Py(111) peaks with Laue oscillations indicating a high degree of structural order.

The polarized neutron reflectivity measurements were carried out on the Magnetism Reflectometer at beamline 4A of the Spallation Neutron Source, Oak Ridge National Laboratory [27]. The diffuse background was subtracted to obtain the true reflectivity. The samples were first measured at 300 K (above the CoO Néel temperature) in the unbiased state in a 1.15 T in-plane magnetic field. They were then cooled down in a 1.15 T or -1.15 T cooling field to 5 K to establish the biased state. The field was cycled three times between ±1.15 T after cooling to minimize any training effects. The reflectivity was measured at both positive and negative saturation states. To measure the reflectivity in the negative saturation state without depolarizing the neutrons, the following methods were applied. (a)

Measuring at a slightly positive magnetic field after applying a negative saturation field to the sample. (b) Warming up the sample and reversing the direction of the cooling field. The results of the two methods are the same.

To fit the polarized neutron reflectivity, a Parratt-type formalism was used. The nuclear and magnetic parts of the scattering length density profile were uncoupled in the fitting program. The nuclear part was constrained by the Cu K_α x-ray reflectivity fitted parameters (Table I) because the x-ray measurements extended to larger Q_z and thus give a better resolution in the structural depth profile. Only the magnetic depth profile was fitted to the polarized neutron data.

The hysteresis loops of both polycrystalline and epitaxial films were measured by a vibrational sample magnetometer (VSM) (Figure 4.1). The measuring conditions and the cooling procedure were the same as that in the neutron experiment.

4.4 Results

The hysteresis loop results (Figure 4.1) are consistent with the previous results of Gökemeijer et al. [10] The polycrystalline sample has a larger exchange bias field (H_E) of 87 Oe and a H_C of 178 Oe, while the (111) epitaxial film has a smaller H_E of 45 Oe but a much larger H_C of 338 Oe. There is a small increase in the saturation magnetization at 5 K compared to that at 300 K, which results mainly from the temperature dependence of the Py moment. In addition, small vertical shifts of the loops are observed at low temperature in both samples, which are attributed to the NS spins, which can exist either at the interface or within the layer [28, 29, 30]. The vertical shift is determined to correspond to a magnetization of 6.4×10^{-6} emu per unit area of film (emu/cm^2) in the polycrystalline sample and 8.8×10^{-6} emu/cm^2 in the (111)-epitaxial film [Figures 4.1(c) and 4.1(d)]. Notice that the positive values of the vertical shift indicates that the net NS moment is parallel to the cooling field. The neutron diffraction results showed that the magnetic moment of a Co^{2+} in CoO is approximately $3.8\mu_B$ [31]. A (111) Co layer with fully oriented spins in a CoO (111) film can be estimated to be 4.48×10^{-5}

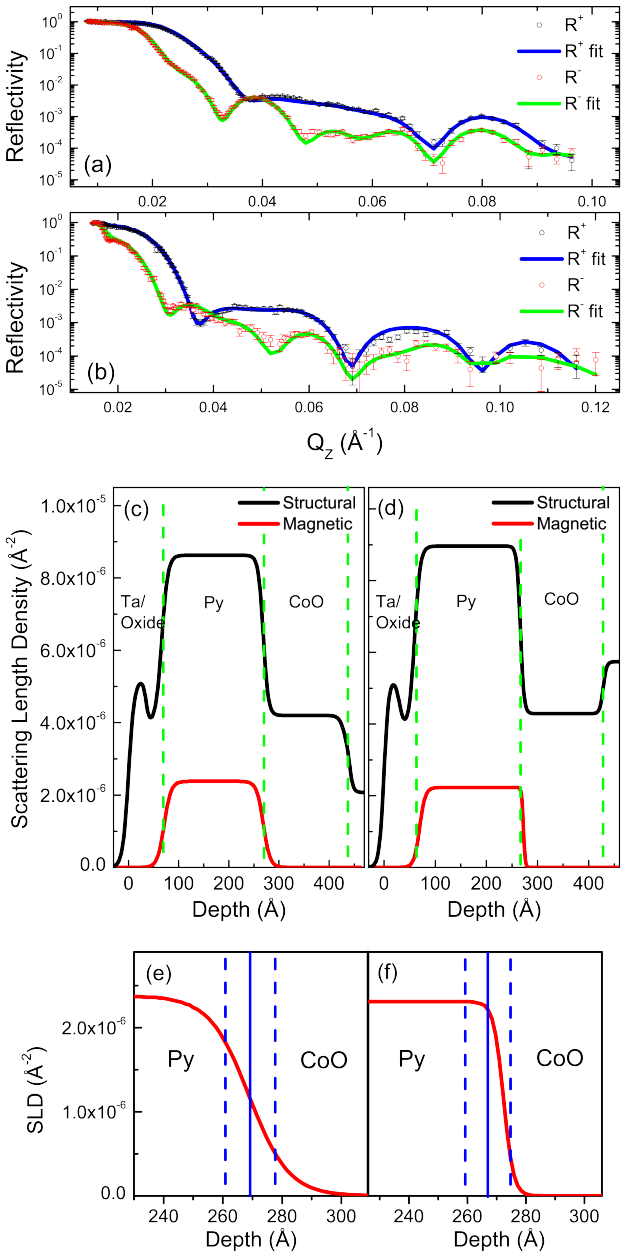

Figure 4.2: Fitted polarized neutron reflectivity data for (a) polycrystalline film and (b) (111) epitaxial film at T = 300 K. The structural and magnetic scattering length density profile extracted from the fitting are shown in (c) and (d) respectively. The green dashed lines define the chemical interfaces. (e) and (f) are magnetic density profiles near the Py/CoO interface for polycrystalline and epitaxial film respectively. The blue solid lines are the chemical interfaces and the dash lines indicate the chemical roughness.

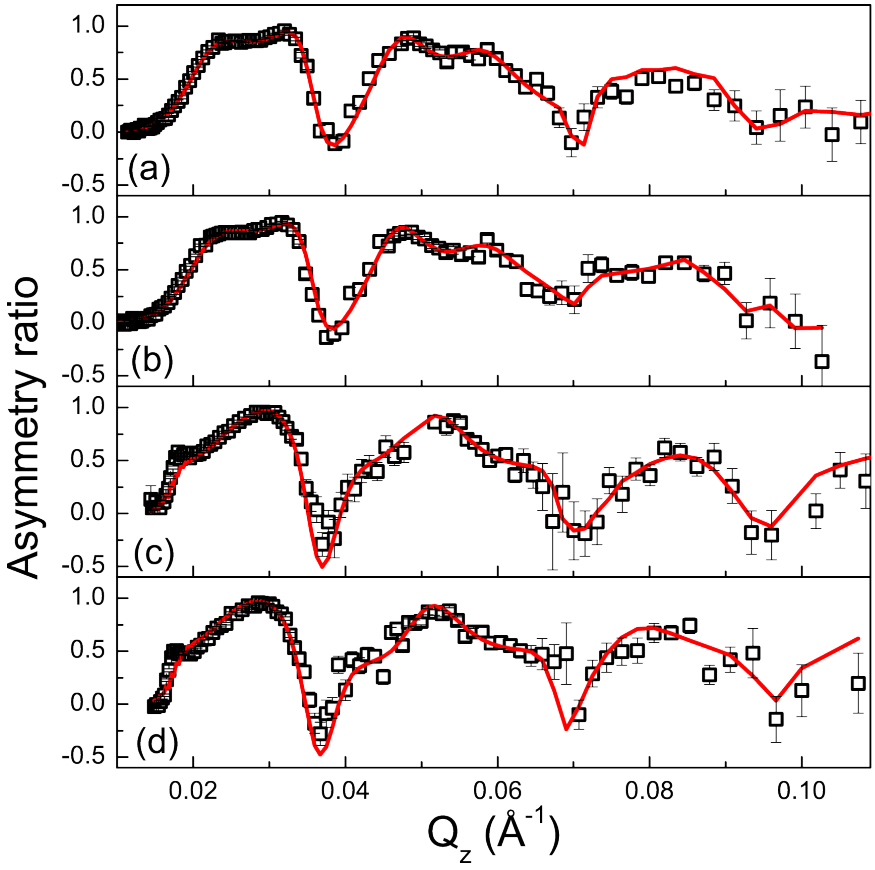

Figure 4.3: Asymmetry ratio calculated from polarized neutron reflectivity. Solid lines are the simulation. (a) polycrystalline film, negative saturation. (b) polycrystalline film, positive saturation. (c) epitaxial film, negative saturation and (d) epitaxial film, positive saturation.

emu/cm^2. Therefore the net NS magnetization is about 13% to 20% of this value. As will be shown later, however, the NS component is not necessarily only from the AFM CoO.

Polarized neutron reflectometry is used to obtain the depth profile of the in-plane magnetization vector [32]. In the reflectometry experiment without the polarization analysis, the measured reflectivities $R^+ = (R^{++} + R^{+-})$ and $R^- = (R^{--} + R^{-+})$ can be individually fitted to obtain information about the magnetization components parallel and perpendicular to the neutron spin. The perpendicular component is relatively small compared to the parallel component in an in-plane saturation field. In the experiment, the neutron spins were always parallel

(spin-up) or anti-parallel (spin-down) to the applied field to maintain the polarization. The scattering length density for spin-up and spin-down can be written as $\rho^{\pm\pm}(z) = \rho_n(z) \pm CM(z)$, with C = 2.853×10^{-9}Å^{-2}cm^3/emu, where ρ_n is the nuclear scattering length density and $M(z)$ is the laterally averaged magnetization at depth z. The chemical thickness and roughness are obtained from x-ray reflectivity, so the nuclear part ρ_n is constrained. For the magnetic part, an interfacial layer between Py and CoO was added which was necessary in order to get a good fit. The magnetic density and the thickness of the Py and the interfacial layer were the fitting parameters, as well as the roughness between the Py/interfacial layer and the interfacial layer/CoO.

Both samples were first measured above the Néel temperature in a saturation field of 1.15 T. Figures 4.2 show the fitted polarized neutron reflectivities at 300 K and the structural/magnetic density profiles extracted from the fitting. At 300 K, both samples showed magnetization profiles different from the nuclear profile at the Py-CoO interface. In the polycrystalline case (Figure 4.2(c)), the magnetic interfacial roughness is much larger ($\sim$ 15 $\mathring{A}$) than the chemical roughness ($\sim$ 7 $\mathring{A}$) and the magnetization extends into the CoO region. For the (111) epitaxial film (Figure 4.2(d)), a magnetic interfacial layer of about 10 $\mathring{A}$ thick is observed, and its width is within the chemical roughness range.

Polarized neutron reflectivity data were then taken in the exchange-biased state for both samples and for positive and negative saturation fields after cooling to 5 K in a 1.15 T cooling field. Figure 4.3 shows the results for the asymmetry ratio, defined as $(R^+ - R^-)/(R^+ + R^-)$, and the simulation from the fitting. $(R^+ - R^-)$ measures the nuclear-magnetic cross term [32] and is very sensitive to the change in magnetization profile. Figures 4.4 (a) and (c) show the magnetic density profiles for the polycrystalline film and the (111) epitaxial film extracted from the fitting. The magnetization of the film in a saturation field can be expressed as:

$$M_{\pm}(z) = M_{NS}^{\pm}(z) \pm M_S(z) \tag{4.1}$$

where $M_{\pm}(z)$ is the laterally averaged magnetization at depth z, the positive (negative) sign is for positive (negative) saturation field. The $M_S(z)$ is the switchable

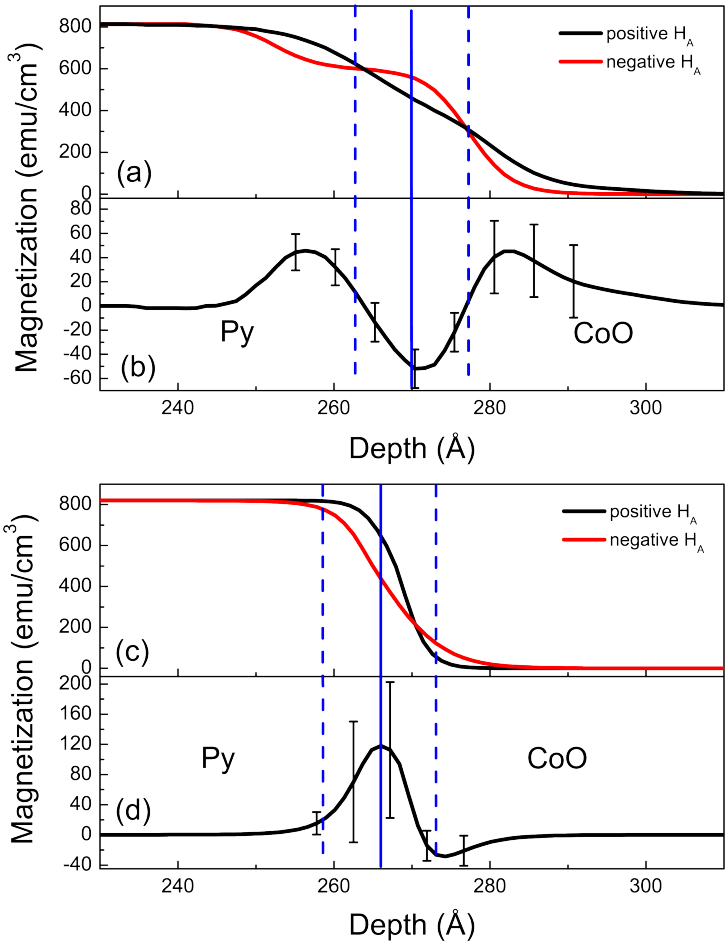

Figure 4.4: Magnetization profiles at T = 5 K extracted from polarized neutron reflectivity fitting. (a) profile of polycrystalline sample and (b) the NS magnetization profile. (c) profile of epitaxial film and (d) the NS magnetization profile. The blue line is the chemical interface and the dashed lines indicate the chemical roughness.

component which completely flips with the magnetic field and the $M_{NS}^{\pm}$ are the NS components in positive and negative saturation fields which include the spins that do not reverse completely with the field. The depth profile of the net NS part is extracted from $[M_{+}(z) + M_{-}(z)]/2$. These are shown for the two samples in Figures 4.4(b) and (d).

Note that these measurements were dominated by the components of the magnetization along the direction of incidence neutron polarization which is in the plane parallel to the film surface. The perpendicular components are relatively small and they would require a measurement of the spin flip reflectivity. These components would be present in the case of a partial domain wall between non-parallel layers of spins, (which would presumably form when the magnetization of the ferromagnet was reversed from the direction of the cooling field) and thus the depth profile into the ferromagnet of the measured $M_{NS}(z)$ from a pinned layer at the interface would appear to have a gradually decaying component. Thus $M_{NS}(z)$ in both ferromagnetic and antiferromagnetic regions are not necessarily fixed magnetization independent of applied field, but could result from the dynamic formation of the partial domain walls upon magnetization reversal. This will be discussed in detail in the discussion section.

a. Polycrystalline film

The NS component of the polycrystalline sample is shown in Figure 4.4(b). In the chemical interfacial region, these moments are anti-parallel to the cooling field, while in the vicinity of the chemical interface, both the Py and CoO regions show NS moments parallel to the cooling field. This shows that the spins across both interfaces are antiferromagnetically coupled to the spins in the interfacial region which is in agreement with the resonant soft x-ray results [24]. NS moments exist in both the Py and CoO region about 20 $\mathring{A}$ on each side, most likely due to partial domain walls originating at the interfaces, as discussed above. At T = 300K (Figure 4.2(c)), we observed that there are magnetic moments extending into the CoO region also about 20 $\mathring{A}$ deep which could be the origin of these NS spins. NS moment profiles were studied in other exchange bias bilayers. Brück et

al. showed that in a MnPd/Fe exchange bias bilayer, the NS Mn moments extend into MnPd about 13 $\mathring{A}$ [33]. More recently, Mohanty et al. observed that in a NiFe/FeMn bilayer, the NS moments exist in both FM and AFM layers [34]. In the case of our polycrystalline Py/CoO system, the NS moment per unit area is estimated to be $+4.9 \times 10^{-6}$emu/cm^2, which has the same order of magnitude as the estimate from the hysteresis loop measurement. The switchable part in the biased state is approximately $M_S(z) = [M_+(z) - M_-(z)]/2$. The ratio between the NS moment to the total moment in the interfacial region is about 10% [35, 24]. Figure 4.5 shows the reflectivity and magnetization of this film at H = 100 Oe after it was saturated at H = -1.15 T. From the hysteresis loop measurement, this is the field where the magnetization is just about to reverse. The magnetization profile (Figure 4.5(b)) shows that the reversal starts from the interface instead of coherently flipping throughout the FM film. This indicates that the reversible spins in the FM layer near the interface have a greater tendency to reverse, as they are experiencing the antiferromagnetic coupling to the switchable spins in the interfacial region.

b. (111)-epitaxial film

The same analysis procedure was applied to the (111) epitaxial film. The magnetization profile (Figure 4.4(c)) shows that, unlike the polycrystalline sample, the variation is confined to the chemical interfacial region. The NS moments (Fig. 4.4(d)) are localized in the interfacial region, parallel to the cooling field near the Py side and antiparallel at the CoO side. The NS per unit area is about $+7.6 \times 10^{-6}$emu/cm^2. The result shows that although the exchange bias is much weaker in an (111) epitaxial film compared to the polycrystalline bilayer, the magnitude of the NS magnetization is greater. However the distribution of NS spins is different. In the polycrystalline film, the NS moments exist in both Py and CoO regions as well as the chemical interface. In the (111) epitaxial film, the NS moments are located at the structural interface and no significant moments are found in the Py and CoO regions. Because the NS moments are only located within a $\sim$ 10 $\mathring{A}$ region and the Q_z-range is limited, the uncertainty of the NS moment

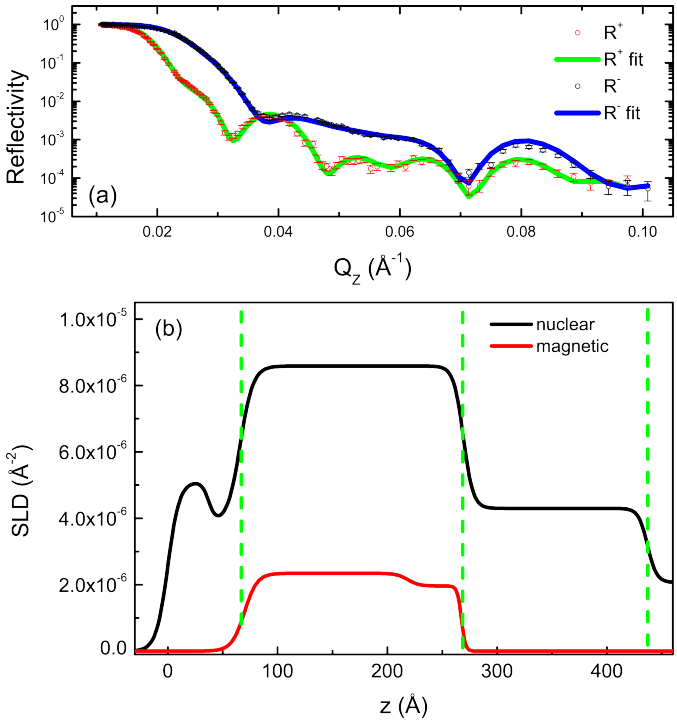

Figure 4.5: (a) Reflectivity fitting and (b) magnetization profile of the polycrystalline film at H = +100 Oe after saturated at H = -1.15 T. The magnetization is just about to reverse. The magnetization profile is flipped for a clearer comparison.

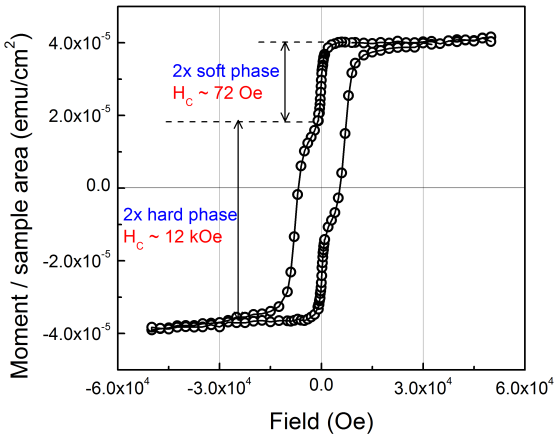

Figure 4.6: The hysteresis loop of a Py(1 nm)/CoO(50 nm) polycrystalline film. Figure is replotted from Figure 3 in reference 25.

profile is relatively large for the epitaxial film. The result also shows that the distribution of the NS moments is highly correlated with the magnetization profile of the unbiased state. In the (111) epitaxial film, we found there is net interfacial magnetization above the Néel temperature within the structural roughness at the interface, and the NS spins are located in the same region in the biased state.

4.5 Discussion

Our previous resonant soft x-ray reflectivity studies [36, 24] demonstrated the existence of an interfacial region of order 10 $\mathring{A}$ in the Py-CoO exchange biased system. At room temperature, above the CoO ordering temperature (T_N), this interfacial region possesses a net magnetization different from that of Py [36]. At 235 K, below T_N, the interfacial layer is still present in the exchange bias state and contains uncompensated Co magnetization, some of which aligns antiparallel to the cooling field, with the major portion oriented parallel to an applied field [24]. The present neutron data shows the distribution of the NS magnetization for both polycrystalline and epitaxial Py-CoO bilayers. This extensive data facilitates the development of a model of the magnetic microstructure of the interfacial region, which is recently discussed in Ref. 25.

The model includes an attempt to reproduce and characterize the ~ 10 $\mathring{A}$ interfacial region, and to examine its influence on the properties of the bilayers with thicker Py. The hysteresis loop of a Py(1 nm)/CoO(50 nm) bilayer, which simulated the interfacial layer, clearly indicates that the interfacial region consists of a very hard magnetic phase and a very soft component (See Figure 4.6) [25]. Further analysis showed that the hard phase was composed of $CoFe_2O_4$ nanoparticles exchange-coupled to the CoO, and that the soft component was composed of nanoparticles that were not exchange-coupled to either the CoO or the Py. Thus, the coupling of the Py to the CoO was mediated by the $CoFe_2O_4$ nanoparticles. The presence of $CoFe_2O_4$ in the interfacial region results from the oxidation/reduction reactions that occur at the interfaces of CoO with Fe, Co, or Ni [37, 38]. It was shown that the dependence of H_C and H_E on Py thickness and on temperature, as well as the magnitude of $\Delta\sigma$ (interfacial energy difference between the two ferromagnetic orientations) in Malozemoffs expression for the exchange interaction [39, 40],

$$H_E = \frac{\Delta\sigma}{2M_S t} \tag{4.2}$$

could be derived from an ~ 10 $\mathring{A}$ interfacial region consisting of $CoFe_2O_4$ and soft nanoparticles, as described above [25]. Since this represents the most comprehensive description of an exchange bias system available, it is pertinent to examine whether this magnetic microstructure of the interfacial region can explain the NS magnetization distributions in Figure 4.4. Consideration of this model [25] recognizes that there is an intermediate layer between the CoO and Py, and that the exchange bias between the CoO and Py layers is mediated by $CoFe_2O_4$ nanoparticles in this layer, i.e., the $CoFe_2O_4$ nanoparticles are pinned to UCS in the CoO and are exchange coupled to the Py spins, thereby transmitting the bias to the Py. The bias is provided by reversible partial domain walls in the CoO at interfaces with the $CoFe_2O_4$ nanoparticles. As discussed above, UCS are responsible for H_E, and it was shown that the uncompensated spin density is inversely proportional to AFM crystallite size [9]. A higher H_E is therefore expected with polycrystalline as compared with epitaxial CoO as a consequence of the higher uncompensated spin density. It is relevant to note that Radu, et al. [22] concluded that UCS are

responsible for H_E also in their (111) epitaxial bilayer, CoO(200 nm)-Py(12 nm). The temperature dependencies of H_E and H_C in that bilayer were the same as for the polycrystalline samples in Ref. 25. H_E was smaller in the epitaxial bilayer in Ref. 22 than in our epitaxial bilayer, as expected from lesser constraints on partial walls in the much thicker epitaxial CoO. These comparisons suggest a similar interfacial structure in the epitaxial bilayer as in the polycrystalline one. What remains to be explained is the larger H_C in the epitaxial bilayer. That CoO domain behavior is involved in the epitaxial H_C can be inferred from the much larger value for the 200 nm CoO [22] than in our $\sim$ 20 nm CoO. This indicates some irreversible changes in the epitaxial CoO domain state after applied field reversal. Such changes were indeed found by polarized neutron diffraction studies by Radu, et al [22]. Thus we may conclude that the increased H_C in the epitaxial bilayer is provided by irreversible CoO domain changes as the $CoFe_2O_4$ nanoparticles to which they are coupled are reversed by the applied field. It is expected that such irreversible CoO domain changes are much smaller or absent in the polycrystalline sample due to pinning at the grain boundaries of the CoO crystallites.

There are four cases to be considered, $CoFe_2O_4$-CoO interaction, AFM and FM, with $CoFe_2O_4$-Py interaction, AFM and FM. By inspecting the NS magnetization profile in Figure 4.4(b), it is reasonable to assume both $CoFe_2O_4$-CoO and $CoFe_2O_4$-Py are AFM-coupled. In our model, the NS spins include the following components: (1) Some of the UCS in CoO which are strongly exchange coupled to the bulk CoO spins and are pinned in the cooling field direction. These are the spins which ultimately give rise to the exchange bias. (2) The spins in the ferrite nanoparticles which are AFM-coupled to both Py and CoO spins and are thus antiparallel to the cooling field. (3) The CoO spins at the interface which form partial domain walls between pinned CoO and the ferrite spins. (4) The Py spins at the interface which form partial domain walls between bulk Py and the ferrite spins. Note that there are also unpinned UCS CoO spins and spins in the ferrite nanoparticles that are not coupled to CoO and Py spins. These spins do not contribute to the NS magnetization and are responsible for the enhancement of the coercive field. Figure 4.7 shows the schematics of the NS spin components and the

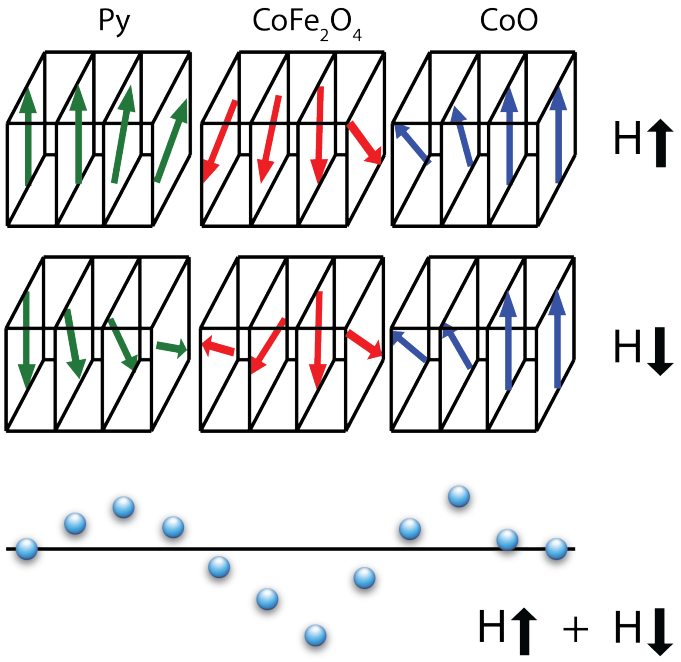

Figure 4.7: The schematic of the spins configuration in the polycrystalline sample in a positive and negative saturation field. Every other plane of the CoO is shown for clarity. The sum of the two (blue spheres) yields the net NS moment profile which reproduces the experimental observation.

sum of H↑ and H↓ reproduces the polycrystalline sum in Figure 4.4(b). The AFM interaction between Py and $CoFe_2O_4$ causes frustration of the Py spins at the interface, which explains why the Py spins at the interface have a greater tendency to reverse. For the epitaxial bilayer, the exchange interaction between CoO and the $CoFe_2O_4$ is again AFM but with a big difference in magnetization profile at the interface from the polycrystalline bilayer. For the epitaxial case, the uncompensated spin density is significantly lower [9] than that in the polycrystalline. Therefore, the epitaxial $CoFe_2O_4$ nanoparticles are the principal components which respond to the cooling field. They were magnetized in the cooling field direction and the adjacent CoO spins adjusted to this condition with AFM coupling, which results in the small negative dip at the CoO interface, as shown in Figure 4.4(b).

In conclusion, both a polycrystalline and a (111) epitaxial Py/CoO bilayer were examined by polarized neutron reflectometry. We confirmed that there are interfacial net magnetic moments above the Néel temperature and the location of the net non-switchable spins are highly related to these spins. The net non-switchable moments in the polycrystalline bilayer exist in both Py and CoO layers and the moments in the epitaxial bilayer are only localized at the interfacial region. A previously proposed model based on a 1 nm interfacial layer consisting of $CoFe_2O_4$ nanoparticles was examined. The non-switchable magnetization profile derived from the model successfully reproduces the profiles in both bilayers assuming an AFM-coupling between the moments in CoO and $CoFe_2O_4$.

This work at UCSD including experiments at ORNL was supported by Basic Energy Sciences, U.S. Dept. of Energy under Grant Number: DE-SC0003678. The text in this chapter is a reprint of the material in S. -W. Chen, X. Lu, E. Blackburn, V. Lauter, H. Ambaye, K. T. Chan, E. E. Fullerton, A. E. Berkowitz and S. K. Sinha. Non-switchable Magnetic Moments in Polycrystalline and (111)-epitaxial Permalloy/CoO Exchange-biased Bilayers, in preparation (2013).

Bibliography

[1] W. H. Meiklejohn and C. P. Bean. New Magnetic Anisotropy. *Physical Review*, 105(3):904, 1957.

[2] J. Nogués and I. K. Schuller. Exchange bias. *Journal of Magnetism and Magnetic Materials*, 192(2):203–232, 1999.

[3] A. E. Berkowitz and K. Takano. Exchange anisotropy – a review. *Journal of Magnetism and Magnetic Materials*, 200(1-3):552–570, 1999.

[4] R. L. Stamps. Mechanisms for exchange bias. *Journal of Physics D: Applied Physics*, 33:R247–R268, 2000.

[5] M. Kiwi. Exchange bias theory. *Journal of Magnetism and Magnetic Materials*, 234(3):584–595, 2001.

[6] J. Nogus, J. Sort, V. Langlais, V. Skumryev, S. Suriach, J. S. Muoz, and M. D. Bar. Exchange bias in nanostructures. *Physics Reports*, 422(3):65 – 117, 2005.

[7] A. E. Berkowitz and R. H. Kodama. In D.L.L. Mills and J.A.C. Bland, editors, *Nanomagnetism: Ultrathin Films, Multilayers and Nanostructures*, Contemporary Concepts of Condensed Matter Science, pages 115–152. Elsevier Science, 2006.

[8] Florin Radu and Hartmut Zabel. Exchange bias effect of ferro-/antiferromagnetic heterostructures. In H. Zabel and S. D. Bader, editors, *Magnetic Heterostructures*, volume 227 of *Springer Tracts in Modern Physics*, pages 97–184. Springer Berlin Heidelberg, 2008.

[9] K. Takano, R. H. Kodama, and A. E. Berkowitz. Interfacial Uncompensated Antiferromagnetic Spins: Role in Unidirectional Anisotropy in Polycrystalline $Ni_{81}Fe_{19}/CoOBilayers. PhysicalReviewLetters, 79(6) : 1130 - -1133, 1997.$

[10] N. J. Gökemeijer and R. L. Penn. Exchange coupling in epitaxial CoO/NiFe bilayers with compensated and uncompensated interfacial spin structures. *Physical Review B*, 63:174422, 2001.

[11] D. Mauri, H. C. Siegmann, P. S. Bagus, and E. Kay. Simple model for thin ferromagnetic films exchange coupled to an antiferromagnetic substrate. *Journal of Applied Physics*, 62(7):3047–3049, 1987.

[12] M. R. Fitzsimmons, P. Yashar, C. Leighton, I. K. Schuller, J. Nogues, C. F. Majkrzak, and J. A. Dura. Asymmetric magnetization reversal in exchange-biased hysteresis loops. *Physical review letters*, 84(17):3986–9, April 2000.

[13] C. Leighton, M. Fitzsimmons, P. Yashar, A Hoffmann, J. Nogués, J. Dura, C. Majkrzak, and I. Schuller. Two-Stage Magnetization Reversal in Exchange Biased Bilayers. *Physical Review Letters*, 86(19):4394–4397, May 2001.

[14] H. Ohldag, T. J. Regan, J. Stöhr, A. Scholl, F. Nolting, J. Lüning, C. Stamm, S. Anders, and R. L. White. Spectroscopic identification and direct imaging of interfacial magnetic spins. *Phys. Rev. Lett.*, 87:247201, Nov 2001.

[15] M. Gierlings, M. Prandolini, H. Fritzsche, M. Gruyters, and D. Riegel. Change and asymmetry of magnetization reversal for a Co/CoO exchange-bias system. *Physical Review B*, 65(9):092407, February 2002.

[16] A. Hoffmann, J. W. Seo, M. R. Fitzsimmons, H. Siegwart, J. Fompeyrine, J.-P. Locquet, J. A. Dura, and C. F. Majkrzak. Induced magnetic moments at a ferromagnet-antiferromagnet interface. *Phys. Rev. B*, 66:220406, Dec 2002.

[17] F. Radu, M. Etzkorn, R. Siebrecht, T. Schmitte, K. Westerholt, and H. Zabel. Interfacial domain formation during magnetization reversal in exchange-biased CoO/Co bilayers. *Physical Review B*, 67(13):134409, April 2003.

[18] M. R. Fitzsimmons, B. J. Kirby, S. Roy, Z. Li, I. V. Roshchin, S. K. Sinha, and I. K. Schuller. Pinned magnetization in the antiferromagnet and ferromagnet of an exchange bias system. *Physical Review B*, 75(21):214412, 2007.

[19] J. Wu, J. S. Park, W. Kim, E. Arenholz, M. Liberati, A. Scholl, Y. Z. Wu, C. Hwang, and Z. Q. Qiu. Direct Measurement of Rotatable and Frozen CoO Spins in Exchange Bias System of CoO/Fe/Ag(001). *Physical Review Letters*, 104(21):3–6, May 2010.

[20] T. J. Moran, J. M. Gallego, and I. K. Schuller. Increased exchange anisotropy due to disorder at permalloy/CoO interfaces. *Journal of applied physics*, 78(3):1887–1891, 1995.

[21] T. J. Moran and I. K. Schuller. Effects of cooling field strength on exchange anisotropy at permalloy/CoO interfaces. *Journal of Applied Physics*, 79(8):5109, 1996.

[22] F. Radu, S. Mishra, I. Zizak, A. Erko, H. Dürr, W. Eberhardt, G. Nowak, S. Buschhorn, H. Zabel, K. Zhernenkov, M. Wolff, D. Schmitz, E. Schierle, E. Dudzik, and R. Feyerherm. Origin of the reduced exchange bias in an epitaxial FeNi(111)/CoO(111) bilayer. *Physical Review B*, 79:184425, 2009.

[23] S. Roy, M. Fitzsimmons, S. Park, M. Dorn, O. Petracic, I. Roshchin, Z.-P. Li, X. Batlle, R. Morales, A. Misra, X. Zhang, K. Chesnel, J. Kortright, S. K. Sinha, and I. K. Schuller. Depth Profile of Uncompensated Spins in an Exchange Bias System. *Physical Review Letters*, 95:047201, 2005.

[24] E. Blackburn, C. Sanchez-Hanke, S. Roy, D. Smith, J. I. Hong, K. Chan, A. Berkowitz, and S. K. Sinha. Pinned Co moments in a polycrystalline permalloy/CoO exchange-biased bilayer. *Physical Review B*, 78(18):180408, 2008.

[25] A. E. Berkowitz, J. I. Hong, S. K. McCall, E. Shipton, K. T. Chan, T. Leo, and D. J. Smith. Refining the exchange anisotropy paradigm: Magnetic and microstructural heterogeneity at the Permalloy-CoO interface. *Physical Review B*, 81(13):134404, 2010.

[26] L. G. Parratt. Surface studies of solids by total reflection of X-rays. *Physical Review*, 95(2):359–369, 1954.

[27] V. Lauter, H. Ambaye, R. Goyette, W.-T. H. Lee, and A. Parizzi. Highlights from the magnetism reflectometer at the {SNS}. *Physica B: Condensed Matter*, 404(17):2543 – 2546, 2009.

[28] J. Nogués, C. Leighton, and I. Schuller. Correlation between antiferromagnetic interface coupling and positive exchange bias. *Physical Review B*, 61(2):1315–1317, January 2000.

[29] H. Ohldag, A. Scholl, F. Nolting, E. Arenholz, S. Maat, A. Young, M. Carey, and J. Stöhr. Correlation between Exchange Bias and Pinned Interfacial Spins. *Physical Review Letters*, 91(1):017203, July 2003.

[30] E. C. Passamani, C. Larica, C. Marques, J. R. Proveti, A. Y. Takeuchi, and F. H. Sanchez. Exchange bias and anomalous vertical shift of the hysteresis loops in milled Fe/MnO2 material. *Journal of Magnetism and Magnetic Materials*, 299(1):11–20, 2006.

[31] W. L. Roth. Magnetic Structures of MnO, FeO, CoO, and NiO. *Phys. Rev.*, 110:1333–1341, 1958.

[32] M. R. Fitzsimmons and C. F. Majkrzak. Application of polarized neutron reflectometry to studies of artificially structured magnetic materials. In Y. Zhu, editor, *Modern Techniques for Characterizing Magnetic Materials*, pages 107–152. Kluwer, Boston, 2005.

[33] S. Brück, G. Schütz, E. Goering, X. Ji, and K. Krishnan. Uncompensated Moments in the MnPd/Fe Exchange Bias System. *Physical Review Letters*, 101:126402, September 2008.

[34] J. Mohanty, A. Persson, D. Arvanitis, K. Temst, and C. Van Haesendonck. Direct observation of frozen moments in the NiFe/FeMn exchange bias system. *New Journal of Physics*, 15(3):033016, March 2013.

[35] J. van Lierop, B. W. Southern, K.-W. Lin, Z.-Y. Guo, C. L. Harland, R. A. Rosenberg, and J. W. Freeland. Exchange bias in a columnar nanocrystalline $ni_{80}fe_{20}$CoO thin film. *Phys. Rev. B*, 76:224432, Dec 2007.

[36] S. Roy, C. Sanchez-Hanke, S. Park, M. Fitzsimmons, Y. Tang, J. Hong, D. Smith, B. Taylor, X. Liu, M. Maple, A. Berkowitz, C. C. Kao, and S. K. Sinha. Evidence of modified ferromagnetism at a buried Permalloy/CoO interface at room temperature. *Physical Review B*, 75:014442, 2007.

[37] R. F. C. Farrow, M. J. Carey, R. F. Marks, P. M. Rice, and D. J. Smith. Enhanced blocking temperature in NiO spin valves: Role of cubic spinel ferrite layer between pinned layer and NiO. *Applied Physics Letters*, 77(8):1191, 2000.

[38] T. J. Regan, H. Ohldag, C. Stamm, F. Nolting, J. Lüning, J. Stöhr, and R. L. White. Chemical effects at metal/oxide interfaces studied by x-ray-absorption spectroscopy. *Physical Review B*, 64(21):214422, November 2001.

[39] A. P. Malozemoff. Random-field model of exchange anisotropy at rough ferromagnetic-antiferromagnetic interfaces. *Phys. Rev. B*, 35:3679–3682, Mar 1987.

[40] A. P. Malozemoff. Mechanisms of exchange anisotropy (invited). *Journal of Applied Physics*, 63(8):3874–3879, April 1988.

5 Diffuse Scattering from a One Dimensional Grating

An infinite homogeneous medium with uniform density only gives rise to scattering intensity at $Q_{||} = 0$. For a planar system, the reflectivity technique discussed in Chapter 4 can be used to obtain the ou-of-plane structural information of the system. The lateral inhomogeneity of the density will give rise to diffuse scattering at $Q_{||} \neq 0$ and in-plane structural information can be obtained by analysing the diffuse scattering data. Grazing incidence small angle scattering utilizes a photon beam which is incident at a very small angle, close to the critical angle of the materials, to obtain the in-plane structural information of the surfaces or interfaces. When the incident angle is comparable to the critical angle, the penetration depth of the light is small so it is surface sensitive, also the scattered intensity is strong. However, the kinematic approximation fails in this regime and a semi-dynamical theory is needed to account for the multiple scattering. The distorted wave Born approximation (DWBA) is one of the most promising methods to solve the small angle scattering problems [1, 2, 3, 4, 5, 6, 7, 8, 9]. Grazing incidence small angle x-ray scattering (GISAXS) is a very commonly used technique to look at in-plane surface structure, especially in looking at periodic structures. A significant effort of calculating GISAXS intensities using DWBA has been carried out over the past two decades and several reviews have been written [10, 11, 12, 13, 14]. The neutron version of this (GISANS) is less reviewed probably because of less experiments have been done due to the relatively weak neutron intensity. However, GISANS can still be a very useful technique in determining magnetic structures. The goal of this work is to develop a diffuse scattering fitting program to analyse

the GISANS data. As a first step, we carried out a GISANS experiment on a one dimensional optical grating as a way to test the DWBA.

In section 5.1, the principles of DWBA will be briefly reviewed. In section 5.2, the experimental details will be discussed. We first show the method of converting the neutron time of flight data to the differential cross section data. Then a calculation based on DWBA is demonstrated and compared to the data.

5.1 Principle of Distorted Wave Born Approximation

In the DWBA theory, we consider the incident wave and the scattered wave as two unperturbed states $|\psi_i\rangle$ and $|\psi_f\rangle$ in an ideal layered system which has sharp interfaces. The roughness in the system is treated as a perturbation in the scattering process. While DWBA is basically a perturbation theory, it might not work well when the perturbation is too large and higher order theory must be applied. In general, DWBA works particularly well when the incident angle is close or below the critical angle while the Born approximation yields a divergent result. At larger Q or higher angles, as will be discussed later, the DWBA is approximately equivalent to the Born approximation and can also be used in this regime.

Some of the following derivation of the DWBA theory is based on the discussion in reference [14]. Consider a multilayer system as shown in Figure 5.1, each layer j has a scattering length density ρ_j and the position of the interface below the layer is z_j. For neutron scattering we start with the Schrödinger equation

$$\left[\frac{\hbar^2}{2m_n}\nabla^2 + V(\mathbf{r})\right]\psi(\mathbf{r}) = E\psi(\mathbf{r}) \tag{5.1}$$

The scattering potential $V(\mathbf{r})$ can be split into two parts

$$V(\mathbf{r}) = \bar{V}(\mathbf{r}) + \delta V(\mathbf{r}) \tag{5.2}$$

The first term corresponds to the unperturbed part which is the layers with sharp

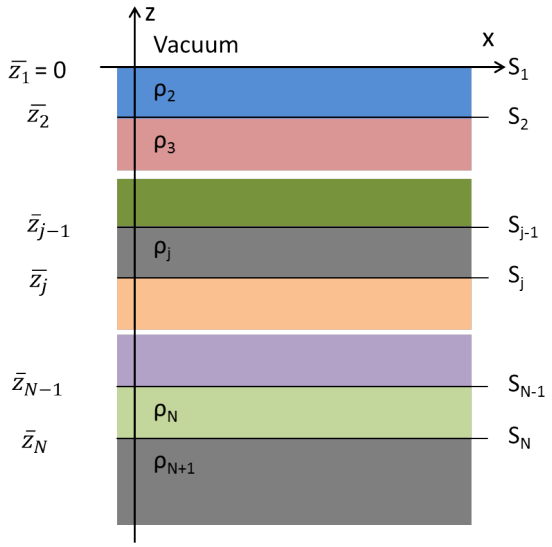

Figure 5.1: Schematic of a multilayer structure.

interfaces, which is given by

$$\overline{V}(\mathbf{r}) = 4\pi \sum_{j=1}^{N+1} \rho_j W_j(\mathbf{r}) \tag{5.3}$$

with

$$W_j(\mathbf{r}) = \begin{cases} 1, & \overline{z}_j < z < \overline{z}_{j-1} \\ 0, & \text{elsewhere} \end{cases} \tag{5.4}$$

The second term is the perturbation from the sharp interface and can be presented as the height fluctuation $\delta z_j(x, y)$,

$$\delta V(\mathbf{r}) = 4\pi b \sum_{j=1}^{N} \Delta\rho_j P_j(\mathbf{r}) \tag{5.5}$$

with

$$P_j(\mathbf{r}) = \begin{cases} 1, & \overline{z}_j < z < \overline{z}_j + \delta z_j(x,y) \quad \text{for} \quad \delta z_j(x,y) > 0 \\ -1, & \overline{z}_j + \delta z_j(x,y) < z < \overline{z}_j \quad \text{for} \quad \delta z_j(x,y) < 0 \\ 0, & \text{elsewhere} \end{cases} \tag{5.6}$$

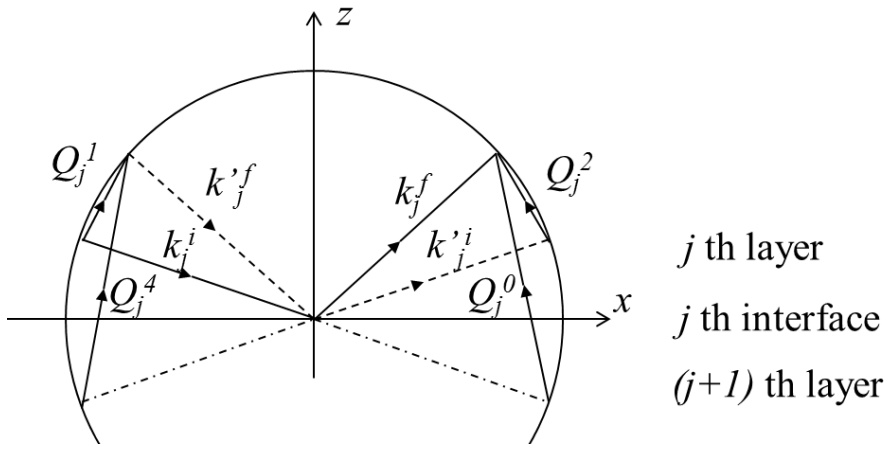

Figure 5.2: Schematic of DWBA wave vectors.

Assume a plane wave $\phi_i = e^{i\mathbf{k}_i\cdot\mathbf{r}}$ is incident on the surface of the multilayer, the unperturbed eigenstates in the jth layer can be shown [2] to be

$$|\psi_{i,j}(\mathbf{r})\rangle = T_j^i(z)e^{i\mathbf{k}_j^i(z)\cdot\mathbf{r}} + R_j^i(z)e^{i\mathbf{k'}_j^i(z)\cdot\mathbf{r}} \tag{5.7}$$

$$|\widetilde{\psi}_{f,j}(\mathbf{r})\rangle = T_j^{*f}(z)e^{i\mathbf{k}_j^{*f}(z)\cdot\mathbf{r}} + R_j^{*f}(z)e^{i\mathbf{k'}_j^{*f}(z)\cdot\mathbf{r}} \tag{5.8}$$

where the eigenstate in equation (5.8) is the time reversed state of a plane wave incident on the surface with the scattered angle. $\mathbf{k}_j^i$ and $\mathbf{k}_j^f$ denote the incident and scattered wavevectors, $\mathbf{k}_j^{'i}$ and $\mathbf{k}_j^{'f}$ are the reflected wavevectors as shown in Figure 5.2. $T_j(z)$ and $R_j(z)$ are the transmission and reflection coefficients in the jth layer which can be obtained by applying Parratt recursive method as shown in section 2.3.

Based on the perturbation theory, the transition matrix is written as

$$\langle f|T|i\rangle \approx \underbrace{\langle\widetilde{\psi}_f|\overline{V}|\phi_i\rangle}_{\overline{V}_{i\to f}} + \underbrace{\langle\widetilde{\psi}_f|\delta V|\psi_i\rangle}_{\delta V_{i\to f}} \tag{5.9}$$

and the differential cross section can be calculated using Fermi's golden rule:

$$\frac{d\sigma}{d\Omega} = \frac{\langle|\langle f|T|i\rangle|^2\rangle_E}{16\pi^2} = \frac{\langle|\overline{V}_{i\to f} + \delta V_{i\to f}|^2\rangle_E}{16\pi^2} \tag{5.10}$$

where $\langle ... \rangle_E$ is the ensemble average of all the roughness configurations. Equation (5.10) can be decomposed into a specular and a diffuse part, where the specular part is from the averaged density and the diffuse part is the deviation from the average:

$$(\frac{d\sigma}{d\Omega})_{\text{spec}} = \frac{|\overline{V}_{i\to f} + \langle \delta V_{i\to f} \rangle_E|^2}{16\pi^2} \tag{5.11}$$

$$(\frac{d\sigma}{d\Omega})_{\text{diff}} = \frac{\langle |\delta V_{i\to f}|^2 \rangle_E - |\langle \delta V_{i\to f} \rangle_E|^2}{16\pi^2} \tag{5.12}$$

In the experiments, the specular part usually is measured up to a high Q, way beyond the critical Q_z where the DWBA does not work very well. A Parratt type calculation is thus more suitable for analysing the specular part. The diffuse part is mainly collected in the vicinity of the critical angle where the DWBA works very well. Also, the averaged fluctuation in density is zero in many cases which makes the second term in Equation (5.12) vanishes which simplifies the calculation. The deviation part of the matrix $\delta V_{i\to f}$ can be written as:

$$\delta V_{i\to f} \approx 4\pi \sum_{j=1}^{N} \Delta\rho_j \sum_{m=0}^{3} G_{j+1}^m F_j(\mathbf{Q}_{j+1}^m) \tag{5.13}$$

with

$$F_j(\mathbf{Q}_{j+1}^m) = \int_{A_j} dxdy \int_{\overline{z}_j}^{\overline{z}_j + \delta z_j(x,y)} dz e^{-i\mathbf{Q}_{j+1}^m \cdot \mathbf{r}} \tag{5.14}$$

This is similar to the form factor in the Born approximation with different Q components. The four $Q's$ are defined as (See Figure 5.2):

$$\begin{aligned}
\mathbf{Q}_j^0 &= \mathbf{k}_j^f - \mathbf{k}_j^i = (\mathbf{Q}_{||}, Q_{z,j}^0) = (\mathbf{Q}_{||}, k_{z,j}^i + k_{z,j}^f), \\
\mathbf{Q}_j^1 &= \mathbf{k}_j^{'f} - \mathbf{k}_j^i = (\mathbf{Q}_{||}, Q_{z,j}^1) = (\mathbf{Q}_{||}, k_{z,j}^i - k_{z,j}^f), \\
\mathbf{Q}_j^2 &= \mathbf{k}_j^f - \mathbf{k}_j^{'i} = (\mathbf{Q}_{||}, Q_{z,j}^2) = (\mathbf{Q}_{||}, -Q_{z,j}^1), \\
\mathbf{Q}_j^3 &= \mathbf{k}_j^{'f} - \mathbf{k}_j^{'i} = (\mathbf{Q}_{||}, Q_{z,j}^3) = (\mathbf{Q}_{||}, -Q_{z,j}^0).
\end{aligned} \tag{5.15}$$

and the four G-factors are the combinations of transmission and reflection coefficients of each layer:

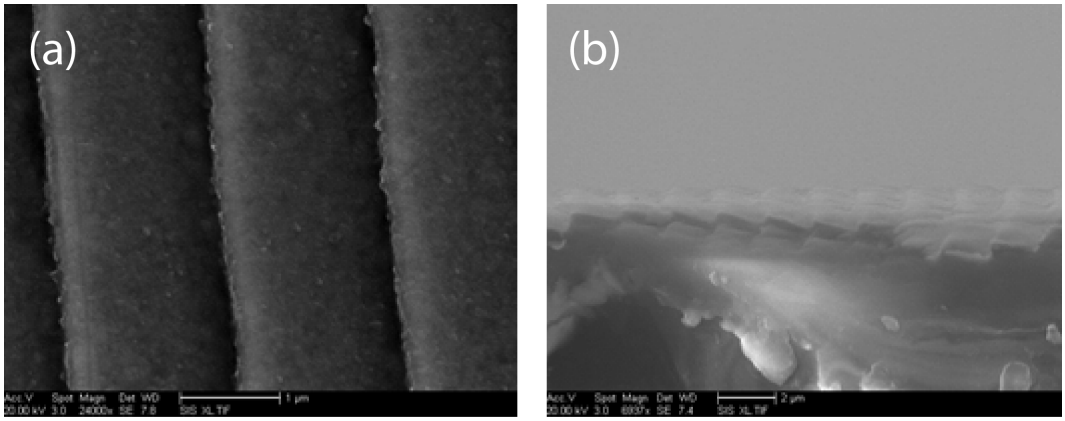

Figure 5.3: Scanning electron microscopy images of the one dimensional sawtooth grating. (a) Top view and (b) side view.

$$\begin{aligned} G_j^0 = T_j^f T_j^i, G_j^1 = R_j^f T_j^i, \\ G_j^2 = T_j^f R_j^i, G_j^3 = R_j^f R_j^i, \end{aligned} \tag{5.16}$$

The full expression of the differential cross section is therefore

$$(\frac{d\sigma}{d\Omega})_{diff} \simeq \left| \sum_{j=1}^{N} \Delta\rho_j \sum_{m=0}^{3} G_{j+1}^m F_j(\mathbf{Q}_{j+1}^m) \right|^2 \tag{5.17}$$

The DWBA theory works very well when $Q_z\sigma \ll 1$. At large Q_z, the roughness morphology becomes very important and can no longer be treated as perturbation. However, in this regime, the reflection coefficients decay rather quickly and the transmission coefficients approach unity. In this case the $T_j^i T_j^f$ term dominates and equation (5.17) and only G_{j0}, Q_{j0} term survives. Therefore the DWBA is approximately equal to the Born approximation.

5.2 Experiments and Results

In order to test the validity and feasibility of applying DWBA for GISANS, a one dimensional optical grating with known structure was used in our experiment. The grating is made of aluminum and is coated on a Pyrex glass substrate and has a sawtooth-shaped unit with period of $\sim 1700\ nm$. In the experiments, the

grating was rotated azimuthally to adjust the period along the beam direction. The images of the grating taken by scanning electron microscope are shown in Figure 5.3. The height of the sawtooth is about 370 nm. The experiment was carried out at the Surface Profile Analysis Reflectometer (SPEAR) beamline at Lujan Neutron Scattering Center (LANSCE) in Los Alamos National Laboratory. SPEAR is a time of flight (TOF) reflectometer with two choppers defining a typical neutron wavelength between 1.5 $\mathring{A}$ to 16 $\mathring{A}$. A one dimensional position sensitive detector was 3.67 m downstream the sample to collect the TOF data. The detector consists of 256 pixels with a pixel size of about 0.78 mm. A schematic of the experimental setup is shown in Figure 5.4.

5.2.1 Data Conversion

The first step is to convert the TOF data to the differential cross section in order to compare with the calculation. The slits were opened wide in the y-direction therefore only x and z components were considered. The differential cross section is written as

$$\frac{d\sigma}{d\Omega}(Q_x, Q_z) = \frac{I(Q_x, Q_z)}{\Phi(\lambda)\Delta\lambda d\Omega} \tag{5.18}$$

where $\Phi(\lambda)$ is the incident neutron flux and $\Phi(\lambda)\Delta\lambda$ can be obtained by measuring the air spectrum.

In a TOF measurement, the intensity is measured in the neutron wavelength (λ) and scattered angle (β) channels. In the geometry shown in Figure 5.4, (λ, β) corresponds to (Q_x, Q_z) through the relation

$$Q_x = \frac{2\pi}{\lambda}\left[\cos(\alpha + \delta\beta) - \cos\alpha\right] \tag{5.19}$$

$$Q_z = \frac{2\pi}{\lambda}\left[\sin\alpha + \sin(\alpha + \delta\beta)\right] \tag{5.20}$$

with

$$\delta\beta = \frac{(\Delta/d_2)\sin(\pi/2 - \alpha)}{1 + (\Delta/d_2)\cos(\pi/2 - \alpha)} \tag{5.21}$$

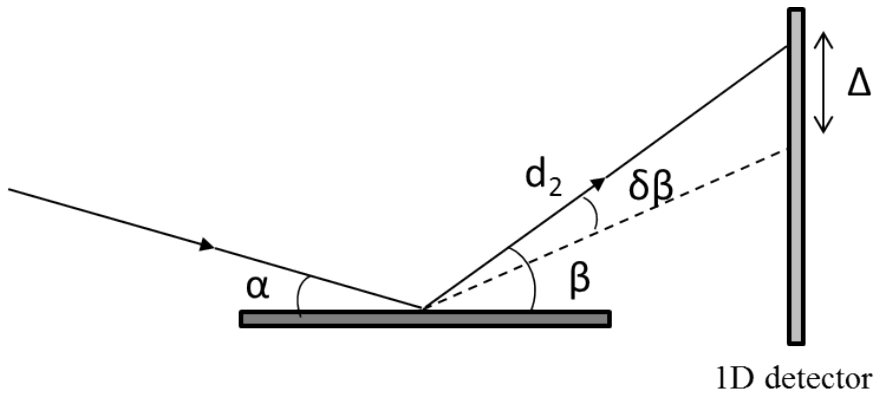

Figure 5.4: Schematic of the experimental setup.

The intensity conversion from (λ, β) space to (Q_x, Q_z) space involves multiplication of a Jacobian determinant $||J||$ defined as:

$$||J|| = \left|\left|\frac{\partial(\delta Q_x, \delta Q_z)}{\partial(\delta\lambda, \delta\beta)}\right|\right| = \frac{2\pi}{\lambda^2}(-Q_x \cos\beta - Q_z \sin\beta) \tag{5.22}$$

Figure 5.5 shows an example of the data conversion. The grating was rotated about 86 degrees azimuthally and the period of the grating is approximately 24 μm along the x-direction in order to obtain diffraction peaks up to the third order. Note that for any azimuthal rotation, it is generally easier to perform the calculation in the sample coordinate then make a transformation into the laboratory coordinate. This will be illustrated in the next subsection.

5.2.2 Differential Cross Section

Equation (5.17) can be used to calculate the differential cross section of the diffuse scattering part. The system consists of four parts: the Pyrex substrate, a flat aluminum film, an aluminum sawtooth grating and an oxide layer on top which has been assumed to be conformal with the grating. In the Born approximation, the differential cross section is simply the Fourier transform of this structure. The calculation based on the Born approximation yields a result shown in Figure 5.6, which fails to reproduce the data shown in Figure 5.5(b). In the DWBA calculation,

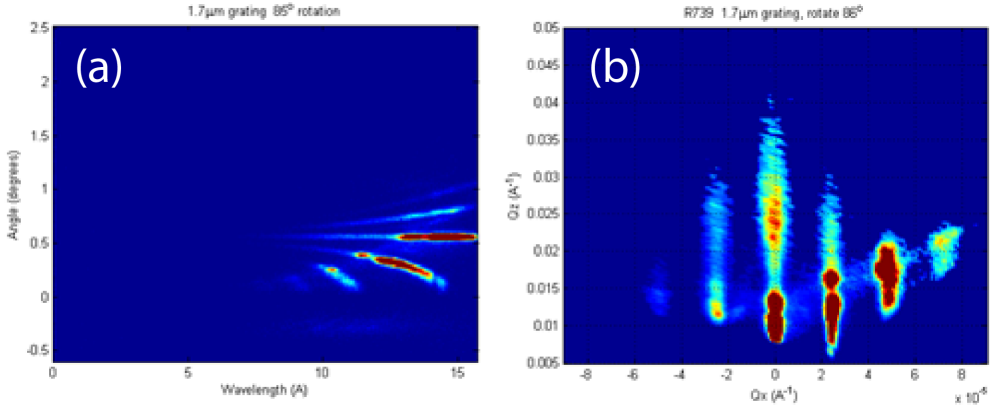

Figure 5.5: (a) Neutron time-of-flight data of the sawtooth grating. The grating was rotated 86 degrees azimuthally and several diffraction rods can be seen. The vertical axis is the scattered angle converted from the detector pixel number. (b) Differential cross section in (Q_x, Q_z) channel converted from (a).

the system is decomposed into three flat layers plus the deviation from the perfect layers, as shown in Figure 5.6. The diffuse scattering is therefore only from the deviation part. A unit of the deviation part is shown in Figure 5.7(b).

We first calculate the form factor part $F_j(\mathbf{Q}^m_{j+1})$ in the deviated layer. It is simpler to calculate in the sample reference frame, meaning the grooves are along the x-direction. For any wave vector $\mathbf{Q}'$ in this reference frame, the form factor can be written as

$$\begin{aligned} F_j(\mathbf{Q}') = \frac{i}{Q'_z}\{ &\Big[\rho_1 - \rho_3 e^{-iQ'_z(h+\Lambda)}\Big] \int dxdy\ e^{-i(Q'_x x + Q'_y y)} \\ &+ [\rho_2 - \rho_1] \int dxdy\ e^{-iQ'_z z_1(x,y)} e^{-i(Q'_x x + Q'_y y)} \\ &+ [\rho_3 - \rho_2] \int dxdy\ e^{-iQ'_z z_2(x,y)} e^{-i(Q'_x x + Q'_y y)}\} \end{aligned} \tag{5.23}$$

with $\rho_1 = \rho_{air} - \rho_{ave}$, $\rho_2 = \rho_{Al_2O_3} - \rho_{ave}$ and $\rho_3 = \rho_{Al} - \rho_{ave}$. $z_1(x, y)$ is the height profile of the aluminum sawtooth and z_2 is the height profile of the oxide. Assuming the oxide layer is conformal with the grooves, $z_2 = z_1 + \Delta$. Because the grating is periodic along the x-direction, the lattice sum can be calculated independently and we only need to consider one unit cell in Equation (5.23). With an azimuthal

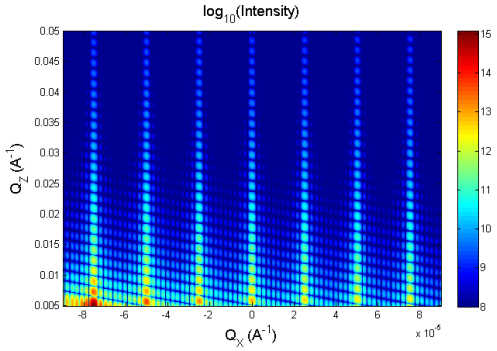

Figure 5.6: Differential cross section calculation based on the Born approximation.

rotation ϕ, the expression can be easily transformed into the laboratory reference frame:

$$\begin{aligned} F_j(\mathbf{Q}) = \frac{i}{Q_z}\{[\rho_1 - \rho_3 e^{-iQ_z(h+\Lambda)}] \int dxdy\ e^{-iQ_x(x\cos\phi + y\sin\phi) - iQ_y(-x\sin\phi + y\cos\phi)} \\ + [\rho_2 - \rho_1] \int dxdy\ e^{-iQ_z z_1(x,y)} e^{-iQ_x(x\cos\phi + y\sin\phi) - iQ_y(-x\sin\phi + y\cos\phi)} \\ + [\rho_3 - \rho_2] \int dxdy\ e^{-iQ_z z_2(x,y)} e^{-iQ_x(x\cos\phi + y\sin\phi) - iQ_y(-x\sin\phi + y\cos\phi)}\} \end{aligned} \tag{5.24}$$

where $\mathbf{Q}$ is any reciprocal space vector in the laboratory reference frame.

In the experiment, the slits are wide open in the y-direction and the integration over the whole wave vector spectrum Q_y yields

$$\int dQ_y \Rightarrow (\sec\phi)\delta(y - x\tan\phi) \tag{5.25}$$

and

$$\begin{aligned} F_j(\mathbf{Q}) = \frac{i\sec\phi}{Q_z}\{[\rho_1 - \rho_3 e^{-iQ_z(h+\Lambda)}] \int_0^\Lambda dx\ e^{-iQ_x x\sec\phi} \\ + [\rho_2 - \rho_1] \int_0^\Lambda dx\ e^{-iQ_z z_1(x,y)}\ e^{-iQ_x x\sec\phi} \\ + [\rho_3 - \rho_2] \int_0^\Lambda dx\ e^{-iQ_z z_2(x,y)}\ e^{-iQ_x x\sec\phi}\} \end{aligned} \tag{5.26}$$

z_1 in a sawtooth profile shown in Figure 5.6(b) can be written as

$$z_1(x) = \begin{cases} x\tan\theta - h, & \text{when } 0 < x < h\cot\theta \\ \frac{-h}{\Lambda - h\cot\theta}(x - \Lambda) + \frac{h^2\cot\theta}{\Lambda - h\cot\theta}, & \text{when } h\cot\theta < x < \Lambda \end{cases} \tag{5.27}$$

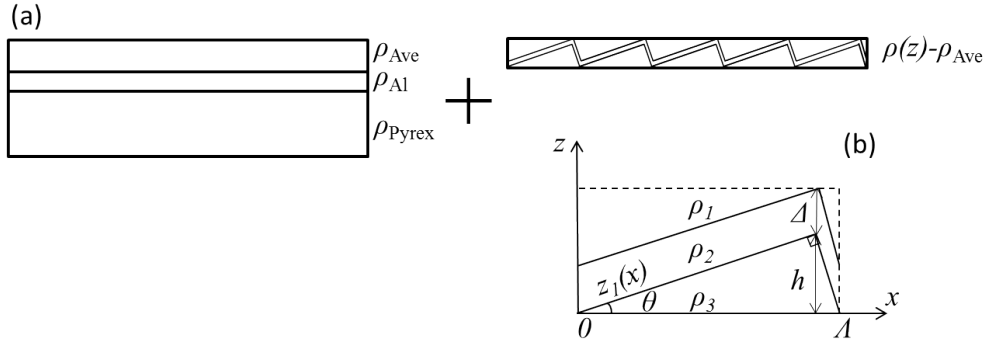

Figure 5.7: (a) The sawtooth grating can be decomposed into a multilayer with uniform density plus the deviation part. Based on DWBA, the diffuse scattering is only from the deviation part. (b) A unit cell of the deviation part.

The form factor therefore has an analytical solution of

$$\begin{aligned} F_j(\mathbf{Q}) = \frac{i\sec\phi}{Q_z}\{&[\rho_1 - \rho_3 e^{-iQ_z(h+\Lambda)}]\delta(Q_x) \\ &+ [(\rho_2 - \rho_1) + (\rho_3 - \rho_2)\ e^{iQ_z\Lambda}] \int_0^\Lambda f[z_1(x)]\ dx\} \end{aligned} \tag{5.28}$$

with

$$\begin{aligned} &\int_0^\Lambda f[z_1(x)]\ dx = \\ &\qquad i(e^{-i\cdot 2n\pi h\cot\theta/\Lambda} - e^{iQ_z h}) \left[\frac{1}{Q_z\tan\theta + 2n\pi/\Lambda} - \frac{1}{Q_z m + 2n\pi/\Lambda}\right] \end{aligned} \tag{5.29}$$

where $m = -h/(\Lambda - h\cot\theta)$ The lattice sum can be written as

$$\sum_{l=0}^{N-1} e^{il(\sec\phi)Q_x\Lambda} = \frac{e^{iNQ_x\Lambda\sec\phi}}{e^{iQ_x\Lambda\sec\phi}} \frac{\sin[NQ_x\Lambda\sec\phi]}{\sin[Q_x\Lambda\sec\phi]} \tag{5.30}$$

The number of units N is determined by the number of units within the in-plane neutron coherence length.

Q in Equation (5.24) - (5.30) can be any reciprocal lattice vector which in the DWBA case is the four Q vectors defined in Equation (5.15). The in-plane component Q_x is the same for all layers in order to satisfy the boundary condition. The out-of-plane component of each layer j is obtained by

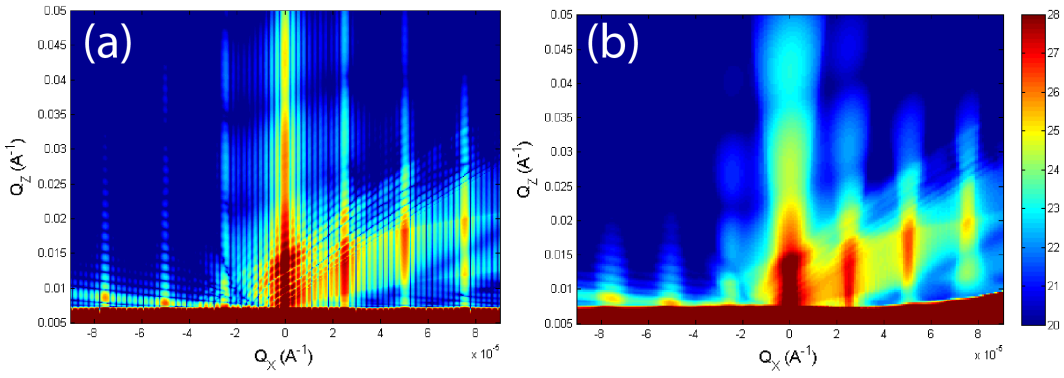

Figure 5.8: (a) Differential cross section of the sawtooth grating calculated with DWBA. (b) Convoluted with instrumental resolution. $\delta\lambda/\lambda$ is 0.01, ($\delta\alpha$ and $\delta\beta$ was estimated by the slits sizes and detector acceptance to be 5.74×10^{-5} and 2.12×10^{-4} respectively.

$$\begin{aligned} Q^0_{2,j} &= k_{0,j}(\sin\alpha_j + \sin\beta_j) = -Q^3_{z,j} \\ Q^1_{2,j} &= k_{0,j}(\sin\alpha_j - \sin\beta_j) = -Q^2_{z,j} \end{aligned} \tag{5.31}$$

where $k_{0,j} = n_j k_0$. α_j and β_j in each layer are obtained by the Snell's law. The refractive index of each layer j is $n_j \sim 1 - \delta_j = 1 - \lambda^2\rho_j/2\pi$.

The four G factors in Equation (5.17) can be obtained by using the Parratt formalism described in Section 2.3, by solving the reflection and transmission coefficient in each layer. Insertion of Equation (5.29) - (5.31) into Equation (5.17), the calculation yields a result for the differential cross section shown in Figure 5.8(a).

5.2.3 Resolution Effect

In a scattering experiment, the measured intensity is an integration of the differential cross section over the detector acceptance solid angle. Many imperfections in the experimental setup cause the resolution effect and corrections have to be taken into account. The effects include finite wavelength spread due to the pre-sample optics, finite divergence of the incident beam, finite acceptance angle of the detector and illuminated sample area etc. [15, 16, 17, 18, 19, 20] All these effects yield dispersed $\mathbf{k}^i$ and $\mathbf{k}^f$ instead of precise values as discussed in the former calculation. The dispersion in $\mathbf{k}^i$ is due to the neutron source, the monochromator,

the focusing optics and the incident slits, while the dispersion in $\mathbf{k}^f$ is from the sample illumination area and the detector acceptance. The uncertainties in $\mathbf{k}^i$ and $\mathbf{k}^f$ result in uncertainties in the wave vector transfer

$$\delta Q_x = \frac{\delta\lambda}{\lambda} Q_x + k(-\delta\beta \sin\cos\chi - \delta\chi \cos\beta \sin\chi + \delta\alpha \sin\alpha)$$

$$\delta Q_y = \frac{\delta\lambda}{\lambda} Q_y + k(-\delta\beta \sin\beta \sin\chi + \delta\chi \cos\beta \cos\chi)$$

$$\delta Q_z = \frac{\delta\lambda}{\lambda} Q_z + k(\delta\beta \cos\beta + \delta\alpha \cos\alpha)$$

(5.32)

where χ is the out-of-plane scattering angle and not in consideration because of the wide opened slit in y-direction.

At a synchrotron x-ray source, the fractional wavelength spread $\Delta\lambda/\lambda$ is smaller than 10^{-4} and does not affect the resolution, while in the neutron TOF instruments, the fractional wavelength spread is usually $\sim 10^{-3} - 10^{-2}$ and the effect has to be taken into account.

The observed intensity at a point $\mathbf{Q}$ is a convolution of the differential cross section and the resolution function [18]

$$I(\mathbf{Q}) = \frac{d\sigma}{d\Omega}(\mathbf{Q}) \otimes \widetilde{R}(\delta\mathbf{Q}) = \int d\mathbf{Q}' \frac{d\sigma}{d\Omega}(\mathbf{Q}') \widetilde{R}(\mathbf{Q} - \mathbf{Q}') \tag{5.33}$$

Generally, the resolution function $R(\delta\mathbf{Q})$ is defined as a Gaussian joint-distribution function of independent random deviations δQ_x, δQ_y and δQ_z

$$\widetilde{R}(\delta\mathbf{Q}) = e^{-\frac{1}{2}\delta\mathbf{Q}\cdot(A^{-1}\delta\mathbf{Q})} \tag{5.34}$$

where $A \equiv [\delta Q_j \delta Q_k]$ is the covariance matrix of the random deviation $\delta\mathbf{Q}$. In many cases, including our experiment, the slits are wide opened in the direction

perpendicular to the scattering plane (xz plane usually) and the integration over the entire wave vector spectrum yields a result independent of that direction, as shown in the previous section. In this case, A is a 2×2 matrix and $\langle \Delta Q_x^2 \rangle$, $\langle \Delta Q_z^2 \rangle$ and $\langle \Delta Q_x \Delta Q_z \rangle$ are assigned to be A_{11}^{-1}, A_{22}^{-1}, A_{12}^{-1} respectively.

The resolution effect results in a smearing of the scattering intensity, which is similar to the finite size effect and the finite coherent volume effect. It is sometimes difficult to distinguish between these effects from one another. For practical reasons the parameters in the resolution function are treated as fitting parameters in the calculation. For example, in the reflectivity measurements described in Chapter 4, the resolution function is of the form $\tilde{R}(Q_z) = e^{-\delta Q_z^2/(2\Delta Q_z^2)}$ and the ΔQ_z is a fitting parameter. In a two dimensional case as described here, estimation of $\Delta\lambda/\lambda$ can be made given the instrumental properties, $\Delta\alpha$ and $\Delta\beta$ can be estimated from the incident and exit slit sizes. An example of the differential cross section (Figure 5.8(a)) convoluted with the resolution function is shown in Figure 5.8(b) and the diffuse scattering calculation qualitatively reproduces the data.

In summary, we carried out a grazing incidence small angle neutron scattering experiment on an one dimensional optical grating. Calculations of the scattering differential cross section based on the Born approximation (BA) and the distorted wave Born approximation (DWBA) were discussed. The results show that the BA fails completely to reproduce the data while the DWBA yields a qualitatively correct result. A quantitative calculation must take into account the roughness on every interface which is beyond the scope of the discussion here.

The content of this chapter is an ongoing project with great help from Jarek Majewski and Michael Jablin in Los Alamos National Laboratory. The extension of the work is in collaboration with Prof. Ivan Schuller, Carlos Monton, Juan Pereiro Viterbo and Ilya Valmianski.

Bibliography

[1] George H. Vineyard. Grazing-incidence diffraction and the distorted-wave approximation for the study of surfaces. *Phys. Rev. B*, 26:4146–4159, Oct 1982.

[2] S. K. Sinha, E. B. Sirota, S. Garoff, and H. B. Stanley. X-ray and neutron scattering from rough surfaces. *Phys. Rev. B*, 38:2297–2311, Aug 1988.

[3] R. Pynn. Neutron scattering by rough surfaces at grazing incidence. *Phys. Rev. B*, 45:602–612, Jan 1992.

[4] V. Holy, J. Kube˘na, I. Ohlidal, K. Lischka, and W. Plotz. X-ray reflection from rough layered systems. *Phys. Rev. B*, 47:15896–15903, 1993.

[5] V. F. Sears. Generalized distorted-wave born approximation for neutron reflection. *Phys. Rev. B*, 48:17477–17485, Dec 1993.

[6] V. Holý and T. Baumbach. Nonspecular x-ray reflection from rough multilayers. *Phys. Rev. B*, 49:10668–10676, Apr 1994.

[7] J.-P. Schlomka, M. Tolan, L. Schwalowsky, O. H. Seeck, J. Stettner, and W. Press. X-ray diffraction from si/ge layers: Diffuse scattering in the region of total external reflection. *Phys. Rev. B*, 51:2311–2321, Jan 1995.

[8] G. Ljungdahl and S. W. Lovesey. Surface scattering near grazing angles: The distorted wave born approximation for rough surfaces. *Physica Scripta*, 53:734–748, 1995.

[9] M. Rauscher, T. Salditt, and H. Spohn. Small-angle x-ray scattering under grazing incidence: The cross section in the distorted-wave born approximation. *Phys. Rev. B*, 52:16855–16863, Dec 1995.

[10] R. Lazzari. IsGISAXS: a program for grazing-incidence small-angle X-ray scattering analysis of supported islands. *Journal of Applied Crystallography*, 35(4):406–421, 2002.

[11] S. Narayanan, D. R. Lee, R. Guico, S. K. Sinha, and J. Wang. Real-Time Evolution of the Distribution of Nanoparticles in an Ultrathin-Polymer-Film-Based Waveguide. *Physical Review Letters*, 94(14):145504, 2005.

[12] G. Renaud, R. Lazzari, and F. Leroy. Probing surface and interface morphology with Grazing Incidence Small Angle X-Ray Scattering. *Surface Science Reports*, 64(8):255–380, 2009.

[13] H. Okuda, M. Kato, K. Kuno, S. Ochiai, N. Usami, K. Nakajima, and O. Sakata. A grazing incidence small-angle x-ray scattering analysis on capped Ge nanodots in layer structures. *Journal of physics. Condensed matter : an Institute of Physics journal*, 22(47):474003, 2010.

[14] Z. Jiang, D. R. Lee, S. Narayanan, J. Wang, and S. K. Sinha. Waveguide-enhanced grazing-incidence small-angle x-ray scattering of buried nanostructures in thin films. *Physical Review B*, 84(7):1–13, 2011.

[15] L. Brgemann, R. Bloch, W. Press, and M. Tolan. Resolution investigations of x-ray three-crystal diffractometers. *Acta Crystallographica Section A*, 48(5):688–692, 1992.

[16] M. F. Toney and D. G. Weisler. Instrumental effects on measurements of surface x-ray diffraction rods: resolution function and active sample area. *Acta Crystallographica Section A*, 49(4):624–642, 1993.

[17] A. Gibaud, G. Vignaud, and S. K. Sinha. The correction of geometrical factors in the analysis of x-ray reflectivity. *Acta Crystallographica Section A*, 49(4):642–648, 1993.

[18] J. S. Pedersen. Resolution effects and analysis of small-angle neutron scattering data. *Le Journal de Physique IV*, 3:491–498, 1993.

[19] W. H. de Jeu, J. D. Shindler, and E. A. L. Mol. The Resolution Function in Diffuse X-ray Reflectivity. *Journal of Applied Crystallography*, 29(5):511–515, Oct 1996.

[20] D. Sentenac, A. N. Shalaginov, A. Fera, and W. H. de Jeu. On the instrumental resolution in X-ray reflectivity experiments. *Journal of Applied Crystallography*, 33(1):130–136, Feb 2000.

6 Conclusions and Prospects

In this thesis, we demonstrate the use of x-ray and neutron scattering techniques to study the magnetic domain wall dynamics and the interfacial spin structures. We also show a calculation based on the distorted wave Born approximation theory to simulate the grazing incidence neutron scattering data. The works are summarized here and possible future research directions are given.

In Chapter 3, we provide evidence of the jamming behavior of domains in a single crystal spiral antiferromagnet. We observe that the domains enter a jammed state as soon as the long range order sets-in. The dynamics show a collective behavior as evidence by compressed exponent 1.5, and exhibit a super Arrhenius behavior that can be described by a Vogel-Fulcher function with a divergence of relaxation time. We also show that the decay constant τ is tied to the domain size. For temperature just below T_N, the domains fluctuate, but increasingly get frozen as the temperature shifts towards T_0. The concept of a jamming transition has not hitherto been applied to magnetic systems but appears to manifest itself in the slow collective dynamics of domain walls below the ordering temperature. Our study shows that domain dynamics near the Néel temperature show many aspects similar to those in supercooled liquids, polymers, colloidal gels, glasses etc. and bolsters the evidence for the universal nature of the jamming transition in discussing the freezing behavior of disordered and frustrated systems. Due to the restriction in time scales for the experiments, the data is somewhat limited in the range of time scales which could be probed for this system. Future experiments are planned on other antiferromagnetic or compensated ferrimagnetic systems which will enable us to look for universal behavior associated with domain growth near the second order phase transition. Similar experiments can also be done with

hard x-ray to look at the bulk properties in these systems. An extremely stable experimental setup is necessary for future works.

In Chapter 4, both a polycrystalline and a (111) epitaxial Py/CoO exchange biased bilayer were examined by polarized neutron reflectometry. We obtained the depth profile of the net non-switchable spins and they are highly correlated with the magnetization depth profile above Néel temperature. The net non-switchable moments in the polycrystalline bilayer exist in both Py and CoO layers and the moments in the epitaxial bilayer are only localized at the interfacial region. A previously proposed model based on a 1 nm interfacial layer consisting of $CoFe_2O_4$ nanoparticles was examined. The non-switchable magnetization profile derived from the model successfully reproduces the profiles in both bilayers assuming an AFM-coupling between the moments in CoO and $CoFe_2O_4$.

Chapter 5 describes a preliminary work in analysing grazing incidence small angle neutron scattering data. A one dimensional sawtooth shaped optical grating was examined to test the validity of the distorted wave Born approximation (DWBA). We show the method of converting the neutron time-of-flight data to the differential cross section data. The DWBA algorithm is briefly reviewed and the calculation qualitatively reproduces the scattering pattern with the consideration of resolution effects. The goal of the project is to develop a data fitting program to analyse the diffuse scattering data from any nanostructure or thin film multilayer. Many works still have to be done to achieve this goal, such as the consideration of the roughness at the interfaces and the domains in the system. Some methods to solve these problems, such as decoupling approximation or local monodisperse approximation, has to be implanted. Furthermore, since DWBA is a perturbation theory, applying a Parratt-type slicing method which decomposes the system into many thin slabs might be a better method to obtain a more reasonable calculation result.

Appendix A
Lateral Domain Size

In the classic paper by Debye, Anderson and Brumberger (*Journal of Applied physics* **28**, 679), those authors derive an expression for the small angle x-ray scattering from a random assembly of voids in a three-dimensional solid, and show that $S(Q)$ is given by

$$S(\vec{Q}) = r_0^2 n_0^2 \Phi(1-\Phi) \int \gamma(\vec{r}) e^{i\vec{Q}\cdot\vec{r}} \mathrm{d}\vec{r} \tag{.1}$$

where r_0 and n_0 are respectively the electron scattering length and the (uniform) electron density of the solid, Φ is the volume fraction of voids, and $\gamma(r)$ is the correlation function. By assuming that the electron density goes from n_0 to 0 as one crosses from the solid region into the void space, and that this crossing is random, Debye et. al. derive the analytical form $exp(-r/a)$ for $\gamma(r)$ which via the Fourier transform leads to the following form for $S(Q)$,

$$S(Q) \sim a^2[1+Q^2a^2]^{-2} \tag{.2}$$

The parameter a is given in terms of the total surface area of the voids, the total volume of the sample and the volume fraction Φ of voids. Since the domains in the Dy film are known to be of cylindrical form in the direction normal to the film, in order to modify their formalism to calculate resonant magnetic scattering from the present system of antiferromagnetic domains in a thin film, we need to change from three dimensions to two. One can show that for a two dimensional system the same argument gives an exponential form for $\gamma(r)$. $S(Q)$ is now the

two-dimensional Fourier transform of $exp(-r/\xi)$,

$$\begin{aligned} I(\vec{Q_{||}}) &\propto \int exp(-r/\xi) exp(i\vec{Q_{||}} \cdot \vec{r}) dS \\ &= \int_0^{2\pi} \int_0^{\inf} exp(-r/\xi) exp(iQ_{||} r\cos(\theta)) r dr d\theta \\ &= \int_0^{\inf} r exp(-r/\xi) J_0(Q_{||} r) dr \end{aligned} \tag{.3}$$

where $J_0(Q_{||}r)$ is the Bessel function. This integral yields

$$S(Q) \sim \xi^2 [1 + Q^2 \xi^2]^{-3/2} \tag{.4}$$

To relate the correlation length to the domain size, we have to consider several different scattering length densities, corresponding to the possible domain orientations in the plane. We note that the scattering length for a single magnetic moment $\vec{m}_i$ in the leading dipole approximation is given by

$$b = \frac{3}{8\pi} \lambda (F_{1-1} - F_{11}) (\vec{e_s} \times \vec{e_i}) \cdot \vec{m}_i \tag{.5}$$

where λ is the wavelength, the F's are resonant matrix elements, and $\vec{e_s}$ and $\vec{e_i}$ are the polarization vectors of the scattered and incident photons respectively. In a given layer, the direction of $\vec{m}_i$ and hence b will change as we cross a domain wall, which for simplicity we assume to be sharp, as for a solid/void interface in a porous solid. We assume the spiraling of the magnets from layer to layer with wavevector Q_m is preserved for all domains (although the chirality might differ) so that the scattering from all domains are centered about (0 ,0, Q_m). We simplify the calculation by assuming only two kinds of domains as in the calculation of Debye et al., which should give us a qualitatively correct result and restrict the calculation to two dimensions. By similar arguments we find that $\gamma(r)$ is still given by $exp(-r/\xi)$ where $\xi = \frac{2A}{L}\Phi(1-\Phi)$. Here A is the total area of the sample and L is the total length of the boundaries between the domains and Φ is the area fraction of one type of domain. In the absence of any detailed information about the domains, we take $\Phi(1-\Phi)$ to be given its average value which is 1/6. If we assume circular domains of one type of radius R, then A/L $\sim$ R so $\xi \sim R/3$, and the domain size is of the order of the diameter or roughly $2R$, yielding $\sim 6\xi$.

Thus by fitting the peaks around (0, 0, Q_m) in the Q_{xy} direction with the above functional form, we can estimate the domain size.

Appendix B
Error Analysis in the Autocorrelation Function

The uncertainty of autocorrelation function g_2 is usually small in the case of multi-speckle method when the intensity (photons per pixel) is large. However, when the intensity is small, the uncertainty can be quite big and the error analysis is necessary to distinguish real signal and the fluctuations in the data. For example, the T = 179.4 K in our dataset. To estimate the uncertainty, one can start from the definition of autocorrelation function and using the uncertainty of the intensity.

The definition of g_2 is given by

$$g_2(Q,\tau) = \frac{1}{N}\sum_{i=1}^{N} \frac{\langle I_i(t_1) I_i(t_1+\tau)\rangle_{t_1}}{\langle I(t_1)\rangle_{t_1}^2} \tag{.6}$$

where i is the index of pixel and N is the total number of pixels in a given Q range. t_1 is the instantaneous time and the τ is the time delayed. In the calculation of g_2, the numerator can be written as,

$$\langle I_i(t_1) I_i(t_1+\tau)\rangle_{t_1} = \frac{1}{M-m}\sum_{n=1}^{M-m} I_i(t_n) I_i(t_{n+m}) \tag{.7}$$

where m is the frame number corresponding to the delayed time and the M is the total number of frames. Thus the deviation of g_2 is,

$$\begin{aligned}\delta g_2(Q,\tau) &\sim \frac{1}{N\langle I(t_1)\rangle_{t_1}^2}\sum_{i=1}^{N}\delta\langle I_i(t_1)I_i(t_1+\tau)\rangle_{t_1} \\ &= \frac{1}{N\langle I(t_1)\rangle_{t_1}^2}\sum_{i=1}^{N}\frac{1}{M-m}\left\{\sum_{n=1}^{M-m}\delta I_i(t_n)I_i(t_{n+m})+I_i(t_n)\delta I_i(t_{n+m})\right\}\end{aligned} \tag{.8}$$

Here we assumed that the deviation of averaged intensity in the denominator is negligible since it is an average over all pixels and all times. Therefore,

$$\begin{aligned}\langle\delta g_2^2(Q,\tau)\rangle = \frac{1}{N^2\langle I(t_1)\rangle_{t_1}^4}\sum_{i}\sum_{n=1}^{M-m}\frac{1}{(M-m)^2} \\ \left\{I_i^2(t_{n+m})I_i(t_n)+I_i^2(t_n)I_i(t_{n+m})+2I_i^2(t_n)I_i(t_{n+m})I_i(t_{n-m})\right\}\end{aligned} \tag{.9}$$

The error bar plotted in the autocorrelation function is the statistical error calculated from the root mean squared error $\sqrt{\langle\delta g_2^2(Q,\tau)\rangle}$.